血管活性腸肽中間神經元於小鼠海馬齒狀回迴路之型態生理學與連接特性

Morpho-Physiological Properties and Connectivity of VIP-Expressing Interneurons in the Mouse Hippocampal Dentate Circuitry

研究生: 衛昱廷 (Yu-Ting Wei)

指導教授: 連正章 博士 (Cheng-Chang Lien, M.D., Ph.D.)

國立陽明大學

神經科學研究所

碩士論文

Institute of Neuroscience

Nation Yang-Ming University

Master Thesis

中華民國 一百零七年 十月

October, 2018

致謝

碩士期間說短不大短，也不好說太長，首先感謝連正章指導教授帶領我進入神經迴路電生理的奧妙小宇宙，除了寬裕的實驗金費協助，最令我敬佩的大概是一對一改論文時，您對於寫作能力及作圖的要求、耐心及改到您肚子每十秒叫一次還沒有丟下我去吃飯。除此之外感謝阿鼠貢獻了他們的身軀，也對不起那些因技術上不純熟或在洗子代時犧牲掉的阿鼠，期望你們的犧牲終將能賦予科學上的意義。

感謝每位指導我或給過我意見的教授、口委、學者及同儕，讓我在這段期間能帶著自己的研究參加歐美知名的兩場研討會見到許多 pioneers。雖然稱不上有多好的獨立研究能力，但至少跟小時候比起來，學會了不少解決問題該有的態度跟科學邏輯。

感恩翁儒韻及劉于超兩位大學長分別給予開放式及紮實式的基礎知識教導，感恩燦廷和政達學長，雖然在實驗室的相處時間不多，但我倒是在你們畢業後常私訊討論實驗上的問題，感恩大鈞在我碩一時，午班在隔壁聽著黃明志一起做電生理聊關於對 endocannabinoid signaling 的熱愛。感恩高敏華帶我了解複雜的 DG networks 並讓我貢獻一己之力於妳的論文。感謝其他所有實驗室夥伴，在實驗或處理雜物上都給予我莫大的幫助，酸離子通道哥小捲、Triple recording 蝦哥、瑞士 CS Flyman、晚班好夥伴抗壓個性好卻難聊的凱誼、頂樓樂天唱歌林昱伶、健身煮飯 GRC 福爾摩斯踢歪歪、IHC 西方點墨王 Jimmy、增加遊戲難度卻勤奮工作的姆姆哈哈、一起買咖啡 Flyman_v2、行為泰拳女 Davis 和有點悲觀的喬治。致未來的學弟妹，希望妳們可多跟實驗室同儕和指導老師討論 Scientific questions 並從跨 Species or brain areas 的討論來凝聚實驗室向心力。

謝謝最後時間裡陪伴我的蹦蹦貓仔、頂樓星空和北投運動中心。感謝家人朋友的一路體諒、援助、陪伴。最後謝謝在天上、對我有養育之恩的外婆，在此對您表達無盡的感激。

各位，因為有你/妳，讓我在此階段有了各層面的成長，感恩感謝珍重

衛昱廷 謹致於

國立陽明大學神經科學研究所

中華民國一百零七年十月

ABSTRACT

The dentate gyrus (DG) acts as an interface between the entorhinal cortex (EC) and hippocampal CA areas. Granule cells (GCs), the principal neurons of the DG, receive fine-tuned inhibition from various types of local GABAerigc interneurons (INs). Compared to other molecularly-defined DG INs, the functional role of vasoactive intestinal peptide (VIP)-expressing INs is poorly understood. Here we show that VIP INs are heterogeneous based on their morpho-physiological and neurochemical properties in the DG. In forty morphologically reconstructed cells, the axons of VIP INs are primarily distributed in the hilus (67.5%, 27 cells) and the remaining cells send their axons exclusively to the molecular layer (ML) (15%, 6 cells), to both the ML and hilus (10%, 4 cells), or to the entire three layers (7.5%, 3 cells). Furthermore, VIP INs display distinct electrophysiological characteristics such as high input resistance (915.6 ± 37.3 MΩ, mean ± SEM, n=106; ranging from 270 MΩ to 1.8 GΩ) and much more depolarized resting membrane potential (-47.6 ± 1 mV, mean ± SEM, n=106; ranging from -26 mV to -69 mV). VIP INs also exhibit heterogeneous discharge patterns, including fast-adapting, regular spiking and irregular spiking. Moreover, approximately 17% VIP INs coexpress calretinin (CR), which mainly send their axons to the hilus and possess fast-adapting discharge patterns. Finally, VIP INs are recruited during the late phase of spike series in response to theta cortical inputs and preferentially innervate INs over GCs and mossy cells (MCs). Collectively, these results suggest that VIP INs are composed of diverse subpopulations and control excitability of the DG via disinhibition.

中文摘要

齒狀回扮演內嗅皮質與海馬迴 CA 區域間的接口。顆粒細胞為齒狀回的主要神經元，主要接收多種 γ-氨基丁酸生成中間神經元的微調抑制。相較於其他分子學定義的中間神經元，表現血管活性腸肽之中間神經元的功能性知之甚少。在此，我們依據型態生理學及神經分子學的特性，發現此類血管活性腸肽之中間神經元具有高度異質性。於四十顆重建細胞中，多數表現血管活性腸肽之中間神經元軸突叢散佈於門區(67 %，27 顆細胞)，然而其餘之血管活性腸肽中間神經元則投射其軸突僅至分子層(15%，6 顆細胞)、跨層於分子層及門區(10%，4 顆細胞)或橫跨於三層(7.5%，3 顆細胞)。除此之外，血管活性腸肽中間神經元顯現不同的電生理特性，如高阻抗(915.6 ± 37.3 MΩ，平均值 ± 平均值標準誤差; 範圍從 270 MΩ 至 1.8 GΩ)及較去極化的靜止膜電位(-47.6 ± 1 mV, 平均值 ± 平均值標準誤差; 範圍從-26 mV 至-69 mV)。血管活性腸肽中間神經元也顯現不同的放電模式，包含快速適應性、不規則性及規則性放電。另外，我們發現約 17 %之血管活性腸肽中間神經元同時表現鈣結合蛋白，並主要投射其軸突至門區並具有快速適應性放電模式。最後，血管活性腸肽中間神經元被激活於晚期的 θ 頻率皮質訊號並主要支配中間神經元而非顆粒細胞及苔癬細胞。這些研究結果顯示血管活性腸肽由不同子群體所組成並經由去抑制作用調控齒狀回之興奮性。

TABLE OF CONTENTS

ABBREVIATIONS

AAV, adeno-associated virus

ACSF, artificial cerebrospinal fluid

AD, adaptation

AHP, afterhyperpolarization potential

AMPA, α-amino-3-hydroxy-5-methyl-4-isoxazolepropionic acid

AP, action potential

BC, basket cell

BLA, basolateral amygdala

C/A, commissural-associational

CB1R, cannabinoid receptor type 1

CCK, cholecystokinin

CeA, central amygdala

ChR2, channelrhodopsin-2

CR, calretinin

Cre, Cre recombinase

CV, coefficient of variation

DAPI, 4',6-diamidino-2-phenylindole

DG, dentate gyrus

EC, entorhinal cortex

eNpHR, enhanced halorhodopsin

EPSC, excitatory postsynaptic current

EPSP, excitatory postsynaptic potential

FAD, fast-adapting

FS, fast-spiking

GABA, γ-aminobutyric acid

GC, granule cell

GCL, granule cell layer

HCA, hierarchical clustering analysis

HICAP, hilar IN with C/A pathway-associated

HIPP, hilar IN with PP-associated

I_c, current clamp

IML, inner molecular layer

IN, interneuron

IPSC, inhibitory postsynaptic current

IRS, irregular spike

IS, interneuron-selective

ISI, inter-spike interval

LPP, lateral perforant pathway

MC, mossy cell

ML, molecular layer

MML, medial molecular layer

MOPP, molecular layer perforant pathway associated

MPP, medial perforant pathway

NGFC, neurogliaform cell

NMDA, N-methyl-D-aspartic acid

OML, outer molecular layer

PC, pyramidal cell

PP, perforant pathway

pSpike, population spike

PV, parvalbumin

R_{in}, input resistance

RMP, resting membrane potential

RS, regular spike

SEM, standard error of mean

SST, somatostatin

Tau (τ), time constants

TML, total molecular layer

TTX, tetradotoxin

uIPSC, unitary inhibitory postsynaptic current

V_c, voltage clamp

VIP, vasoactive intestinal polypeptide

YFP, yellow fluorescent protein

INTRODUCTION

Synaptic Inhibition in the Hippocampus

The interaction between excitation and inhibition orchestrates the information flow through neural networks (Isaacson and Scanziani, 2011). Although inhibitory GABAergic interneurons (INs) are a minority population in the brain, they play an essential role in shaping the spatiotemporal dynamics of network activity, tuning the sensory information and selecting the cell ensembles (Klausberger and Somogyi, 2008; Lapray et al., 2012). Accordingly, it is of paramount importance to understand the functional role of GABAergic INs. The hippocampus is a key cortical component of mammalian brains and serves as a pivotal role in episodic memory, spatial navigation, and stress-related emotional behaviors (Scoville and Milner, 1957; Milner et al., 1968; Fanselow and Dong, 2010; Kheirbek et al., 2013). The hippocampus consists of distinct subfields. Among them, the dentate gyrus (DG) is the first station of hippocampus and relays information from the entorhinal cortex (EC) to CA areas. The principal cells in the DG are granule cells (GCs), which send axons toward downstream CA areas, termed mossy fibers (Kohara et al., 2014). Intriguingly, GCs integrate inputs with low efficiency and generate sparse activity. There are several mechanisms. Firstly, GCs exhibit a relatively hyperpolarized resting membrane potential (RMP) and receive shunting inhibition during action potential (AP) generation (Chiang et al., 2012). Secondly, GCs integrate synaptic inputs linearly and reveal strong dendritic attenuation, resulting inefficient EPSP propagation (Ewell and Jones, 2010; Krueppel et al., 2011) Finally, GCs are tightly controlled by diverse GABAergic INs (Liu et al., 2014; Hsu et al., 2015; Lee et al., 2016). Such sparse firing activity is crucial for contextual learning and pattern separation, providing a gate to

transform cortical information into distinct representations (Leutgeb et al., 2007; Kheirbek et al., 2013).

Diverse GABAergic INs in the DG Microcircuits

The computations of the DG depend on dynamic microcircuits, which are composed of excitatory principal neurons and inhibitory GABAergic INs. The DG INs display a rich diversity in accordance with their morphological, electrophysiological, neurochemical and synaptic characteristics (Freund and Buzsáki 1996; Hosp et al., 2014; Hsu et al., 2015). INs are specialized to innervate different subcellular domains of target neurons, reflecting their unique anatomical features and functions (Halasy and Somogyi, 1993; Markram et al., 2004; Hefft and Jonas, 2005). For instance, perisomatic inhibitory synapses efficiently control the onset of spike whereas dendritic inhibitory synapses regulate synaptic function and plasticity (Miles et al., 1996; Pouille and Scanziani, 2004; Gidon and Segev, 2012). INs also display heterogeneous firing patterns and diverse intrinsic membrane properties such as RMP, afterhyperpolarization potential (AHP), input resistance (R_{in}), AP threshold and half-width (Petilla Interneuron Nomenclature Group et al., 2008; Hosp et al., 2014). Furthermore, INs express different neurochemical markers including Ca^{2+}-binding proteins such as parvalbumin (PV), neuropeptides such as somatostatin (SST) and cholecystokinin (CCK) (Mcbain and Fisahn, 2001). Finally, INs form specific synapses onto their targeting neurons. The various synaptic properties are highly associated with the temporal precision of presynaptic AP and the combinatorial interactions between two neurons (Gupta et al., 2000; Savanthrapadian et al., 2014; Walker et al., 2016)

Like other cortical regions, the DG contains multiple types of INs, which are classified based on their morpho-physiological and neurochemical criteria (Freund and

Buzsáki 1996; Hosp et al., 2014). First of all, PV-expressing basket cells (BC) with the axon plexus predominantly in the granule cell layer (GCL) exhibit fast-spiking (FS) discharge pattern and provide strong perisomatic inhibition onto GCs (Hu et al., 2014). Furthermore, other types of IN mostly terminate on the dendrites of GCs, such as SST-expressing hilar perforant pathway-associated (HIPP)-like cells and CCK-/cannabinoid receptor type 1 (CB1R)- coexpressing hilar commissural associational pathway-associated (HICAP)-like cells, in which axons are innervating in the outer molecular layer (OML) and inner molecular layer (IML), respectively. (Halasy and Somogyi, 1993; Hefft and Jonas, 2005; Savanthrapadian et al., 2014). Moreover, total molecular layers (TML)-like cells with the axonal plexus located in the TML are also immunoreactive for the CB1R (Yu et al., 2015). Finally, molecular layer (ML)-like cells send their neurites toward the entire ML and are subdivided into molecular layer perforant path associated (MOPP) cells and neurogliaform cells (NGFCs) (Armstrong et al., 2011). As a corollary, the spatiotemporal dynamics of GCs are likely controlled by a repertoire of diverse IN subtypes.

IN-Selective INs Mediate Disinhibitory Circuitries

In the neocortical area, vasoactive intestinal polypeptide (VIP)-expressing neurons belong to the ionotropic serotonin receptor $5HT_{3A}$ ($5HT_{3A}R$) class, a major division of neocortical INs in parallel with PV- and SST-expressing INs (Taniguchi et al., 2011; Pfeffer et al., 2013; Prönneke et al., 2015; Karnani et., 2016; Wall et al., 2016). Unlike PV- and SST-expressing INs, VIP INs specialize in targeting other INs and mediate disinhibitory control, thereby reinforcing the sensory inputs in the cortical areas (Lee et al., 2013; Pfeffer, 2013; Pfeffer et al., 2013; Pi et al., 2013; Jackson et al., 2016; Karnani et al., 2016; Walker et al., 2016; Garcia-Junco-Clemente et al., 2017). In addition to

targeting INs, VIP INs directly inhibit pyramidal cells. Notably, the strength of direct inhibition is more pronounced in the frontal cortex but weak in the occipital cortex (Garcia-Junco-Clemente et al., 2017). In the hippocampus, VIP INs project to distinct types of neurons. Calretinin (CR)-expressing VIP INs mainly inhibit INs, whereas VIP-BC, which coexpress CCK, innervate CA1 pyramidal cells or GCs (Acsády et al., 1996; Hájos et al., 1996; Tyan et al., 2014). Taken together, VIP INs are able to directly and indirectly modulate the hippocampal input-output transformation.

An early study revealed that VIP neurons in the DG display a rich diversity in their morphologies (Hájos et al., 1996). However, it was difficult to identify or specifically target VIP INs. Accordingly, no attempt has been made for the detailed characterization of electrophysiological and synaptic properties of the VIP INs subtypes in the DG. To address these unanswered questions, we combined mouse genetics (Madisen et al., 2010; Taniguchi et al., 2011), electrophysiology, immunohistochemistry, single-cell reconstruction and optogenetic-assisted mapping to elucidate the cellular profiles and the connectivity of VIP INs in the mouse DG. Taken together, our results reveal that VIP INs in the mouse DG comprise several distinct subtypes and specialize in inhibiting inhibitory INs.

MATERIALS AND METHODS

Animals

All animals (C57BL/6. B129 background) were handled in accordance with the national and institutional guidelines, and the protocol (#1060428) was approved by the Institutional Animal Care and Use Committee of the National Yang-Ming University. Transgenic mice including VIP-ires-Cre (stock #010908) and Ai14 (stock #007914) lines were obtained from Jackson Laboratory (Bar Harbor, ME, USA). Mice of both sexes were included in this study.

Serial Whole Brain Sections

VIP-ires-Cre::Ai14 mice were perfused with 4% paraformaldehyde (PFA) and the coronal, sagittal and transverse sections of the brain were cut into 60 μm. Slices were mounted with 4',6-diamidino-2-phenylindole (DAPI, H-1500, Vector Labs, Burlingame, CA, USA). Single plane of VIP-tdTomato expression was captured by Research High-Class Stereo Microscope System (SZX16, Olympus, Tokyo, Japan).

Viral Constructs and Stereotaxic Injection

To selectively activate or silence VIP neurons in the DG, we utilized a Cre-inducible channelrhodopsin-2 (ChR2) construct (rAAV5-EF1α-DIO-hChR2(H134R)-eYFP-WPRE-pA) or an enhanced-halorhodopsin (eNpHR) construct (AAV5-EF1α-DIO-eNpHR3.0-eYFP) obtained from the University of North Carolina Core (UNC) vector core (http://www.med.unc.edu/genetherapy/vectorcore).

Mice (at postnatal days >45) were anesthetized with 4 % isoflurane (vol/vol;

Halocarbon Laboratories, North Augusta, SC, USA) in 100% oxygen in the induction chamber (air flow rate: 4 ml/min) (Lee et al., 2013; Hsu et al., 2016) and then the heads were shaved. Mice were placed onto the stereotaxic frame (IVM-3000; Scientifica, Uckfield, UK) and kept under constant flow rate. Animal's mouth and nose were immersed into the mask with sustained isoflurane air flow. A temperature controller (TMP-5b; Supertech, Budapest, Hungary) was placed below the mice to keep the body temperature constant (~36 ˚C). After securing the head with two ear bars, 75% ethanol was used to disinfect the surgical area and the animal's eyes were protected by an ophthalmic gel (Dr. Gerhard Mann Chem-pharm. Fabrik GmbH Brunsbutteler Damm 165-173, 13581 Berlin, Germany). To target the hippocampal DG, a midline scalp incision (~1 cm) was made with scissors and the skin was pulled aside to expose the skull. Small craniotomies [ventral DG, coordinates from Bregma: anteroposterior (AP): -3.4 mm; mediolateral (ML): ±2.8 mm; Dorsal DG, coordinates from Bregma: AP: 2 mm; ML: ±1.3 mm] were made bilaterally. The viral vector was delivered through the craniotomy to the two locations within the hippocampus [ventral DG, dorsoventral (DV): -4.4 and -4.2 mm; Dorsal DG, DV: -2 and 1.8 mm] by using a 10-µl NanoFil syringe (World Precision Instruments, Sarasota, FL, USA) and a 35-gauge beveled metal needle. Injection volume (0.5 µl at each location) and the flow rate (0.1 µl/min) was controlled with a nanopump controller (KD Scientific, Holliston, Massachusetts, USA). After injection, the needle was left for 10 min and was then withdrawn slowly. All animals were allowed at least 3 weeks for complete recovery and sufficient gene expression.

Slice Electrophysiology and Optical Stimulation

Coronal or transverse brain slices of 400 µm thickness were prepared from both *VIP-ires-Cre::Ai14* or AAV-infected VIP-ires-Cre mice using a vibratome (DTK-1000,

Dosaka, Kyoto, Japan). All animals were sacrificed by decapitation. The brains were rapidly removed and slices were cut in ice-cold cutting saline containing (in mM): 87 NaCl, 25 $NaHCO_3$, 1.25 NaH_2PO_4, 2.5 KCl, 10 glucose, 75 sucrose, 0.5 $CaCl_2$ and 7 $MgCl_2$. Brain slices were incubated in the oxygenated (95% O_2/ 5% CO_2) cutting saline for the recovery at 34 ˚C, and stored at the room temperature until used. During the experiments, slices were placed in the recording chamber and perfused with oxygenated artificial cerebral spinal fluid (ACSF) containing (in mM): 125 NaCl, 25 $NaHCO_3$, 1.25 NaH_2PO_4, 2.5 KCl, 25 glucose, 2 $CaCl_2$ and 1 $MgCl_2$.

For the whole-cell recordings, the cells were visually selected for recording under infrared differential interference contrast (IR-DIC) microscope (BX51WI; Olympus). Recordings were performed with Multiclamp 700B amplifier (Molecular Devices, Sunnyvale, CA, USA). Recording electrodes (3-5 MΩ) were pulled from borosilicate glasses with filament (outer diameter, 1.5 mm; wall thickness, 0.32 mm; Harvard Apparatus, Edenbridge, UK). For the measurement of intrinsic properties, glass pipettes were filled with low Cl^- internal solution containing (in mM): 136.8 K-gluconate, 7.2 KCl, 0.2 EGTA, 4 MgATP, 10 HEPES, 7Na_2-phosphocreatine, 0.5 Na_3GTP (pH 7.3 with KOH), and 0.4 % biocytin (wt/vol; Life Technologies, Grand Island, NY, USA). For experiments of ChR2-eYFP-expressing neurons, optogenetic-assisted mapping and paired recording, pipettes were filled with high Cl^- internal solution containing (mM): 15 K-gluconate, 140 KCl, 0.1 EGTA, 2 $MgCl_2$, 4 Na_2ATP, 10 HEPES, 0.5 Na_3GTP and 0.4% biocytin. For cell-attached recording and measurement of inhibitory (I)-excitatory (E) conductance ratio, Cs^--based intracellular solution containing (in mM): 121.5 $CsMeSO_3$, 0.1 EGTA, 4 $MgCl_2$, 13.5 CsCl, 10 HEPES, 5 QX-314 bromide, 2 Na_2ATP, 10 Na_2-phosphoreatine, 0.3 Na_3GTP. For most of the recordings, pipette capacitance was almost fully compensated

and series resistance was compensated to ~80% (Bandwidth: 1-2 kHz) in the voltage-clamp configuration. Signals were low-pass filtered at 4 kHz and sampled at 10 kHz using Digidata 1440A (Molecular Devices). A Digidata 1440A connected to a personal computer was used for stimulus generation data acquisition. Pulse sequences were generated by pClamp 10.2 (Molecular Devices). The measurement of intrinsic properties and PP recruitment were made at 32 ± 1˚C. The remaining experiments were made at 23 ± 2°C.

Cell-attached recording (pipette resistance 5-6 MΩ) was made to detect spike responses during PP stimulation, and the extracellular stimulation electrode (tip diameter ~ 10 μm; filled with ACSF; current clamp) was made for orthodromic stimulation of PP. Trains of stimulation with near-threshold intensities at 10 Hz were delivered every 15 s using a stimulus isolator (Isoflex, A.M.P.I., Jerusalem, Israel). With near-threshold intensities, each train triggered at least one spike in more than 50% of trials and the probability of spike generation triggered by any stimulus did not exceed 0.8 (Pouille and Scanziani, 2004; Liu et al, 2014). Antidromic spikes, distinguished by a lack of spike jitter, were excluded.

For examination of modulatory inputs, puffing pipette (3-4 MΩ) was placed 10-20 μm away from the recorded soma. The cholinergic agonist carbachol (1 mM, 30 ms, ~10-15 psi) was puff applied by using PicoSpritzer III (Parker Hannifin, Cleveland, OH, USA).

For optical stimulation, ChR2 was excited by optical stimuli at 470 nm (driven by DC4104, Thorlabs, Newton, NJ, USA), which was delivered directly through the objective. The optical stimuli were simultaneously recorded by a GaP photodiode (wave length range: 150-550 nm, Thorlabs). Photocurrents recorded from the eYFP expressing neurons and inhibitory synaptic responses were evoked by 5 Hz trains of photostimulation

(light pulse duration, 5 ms, inter-train interval, 15 s). Light intensity was measured by a photometer (5-7 mW in blue light delivering area, Thorlabs). To examine the NpHR effect on VIP neurons, the same approaches were used. Amber light with wavelength 590 nm (500 ms, 2-3 mW) was delivered.

Chemicals and Drugs

To examine the function of ChR2, a sodium channel antagonist tetradotoxin citrate (TTX, 1 μM, Ascent Scientific) was used to isolate photocurrents. For optogenetic-assisted circuit mapping of VIP INs, kynurenic acid (KA, 2 mM, Sigma) was utilized to block AMPA/NMDA receptors. In a subset of experiments, gabazine (SR-95531, 1 μM, Tocris) and CGP35348 (1 μM, Tocris) were used to block the $GABA_A$ and $GABA_B$ receptors, receptively. For puffing experiments, KA (2 mM, Sigma), gabazine (SR-95531, 1 μM, Tocris) and CGP35348 (1 μM, Tocris) were bath applied to block the glutamatergic and GABAergic synaptic transmission.

Immunohistochemistry

For the colocalization between each neuronal marker, *VIP-ires-Cre::Ai14* mice were perfused with 4% PFA and the brain was permeabilized with PFA at 4℃ for 2-6 hours. The DG was cut into 60 μm and washed in 0.1% Triton X-100 in Tris buffered saline (TBS) and then incubated in a blocking solution that containing 5% normal goat serum (SP-1000, Vector Labs, Burlingame, CA, USA) or 1-2X animal-free blocker (SP-5030; Vector Labs, Burlingame, CA, USA) in TBS for 2-4 hours at 23-25℃. Slices were then incubated with primary antibodies in the blocking solution at 4℃ for 24-48 hours (primary antibodies are listed in Table. 1), washed in TBS three times for 10 min each, followed by 2-4 hours of secondary antibody incubation at 23-25°C and washed six times

in TBS for 10 min each. Slices were mounted in Vectashield with DAPI (H-1500, Vector Labs, Burlingame, CA, USA). The detailed protocol is described in the supplementary IHC protocol. Confocal images were acquired sequentially using Leica DM6000 CFS (Leica, Wetzlar, Germany) that was equipped with a 20x/1.0 numerical aperture (NA) water immersion objective (HCX APO L; Leica, Wetzlar, Germany).

Biocytin Filling and *Post-hoc* Morphological Reconstruction

To investigate the morphology of a single cell, the recorded neurons (filled with 0.4 % biocytin) were fixed overnight with 4% PFA in the phosphate-buffered saline (PBS). After washing with PBS 3 times, slices were incubated with streptavidin-conjugated Alexa Fluor 594 or 488 (1:300; Life Technologies, Grand Island, NY, USA) in PBS and 0.2% Triton X-100 (vol/vol; USB Co., Cleveland, OH, USA) overnight at 4°C. After washing with PBS, slices were mounted in Vectashield with DAPI (H-1200, Vector Laboratories, Burlingame, CA, USA). Labelled neurons were examined by a two-photon microscope using a pulsed titanium: sapphire laser (Chameleon-Ultra II tuned to 800 nm for scanning; Coherent, Portland, OR, USA) attached to a Leica DM6000 CFS (Leica, Wetzlar, Germany) that was equipped with a 20x/1.0 numerical aperture (NA) water immersion objective (HCX APO L; Leica, Wetzlar, Germany). In a subset of experiments, labelled neurons and viral expression were imaged using confocal Argon or HeNe laser excitation (Leica, Wetzlar, Germany). For single neuron reconstructions, Image stacks were imported into the Neuromantic 1.6.3 software. Analysis of morphological parameters was performed using Neurolucida Explorer (MBF Bioscience, Williston, VT, USA). To quantify the axonal distribution, we counted the number of intersections made by the axons with lines running parallel to each layer and interspaced by 10 μm (Liu et al, 2014).

Hierarchical Clustering Analysis

For cell clustering, we performed squared Euclidean distances and Ward's method (Ward, 1963). All of the electrophysiological properties of VIP INs were tested by the D'Agostino-Pearson normality test (listed in Fig. 5) and Pearson's correlation test. Features were excluded with the absolute value of correlation greater than 0.7 (listed in Table 5). For the correlation test and hierarchical clustering analysis, each variable was normalized into z-score. The distance between data points represented the dissimilarity between them, closer data points have higher similarity. The color keys in the heatmap represent the $\log_2$-fold change of certain feature in individual cells compared to other cells. To determine the optimal groups (k) of k-means in electrophysiological clustering, we performed average silhouette method (Rousseeuw, 1987) to compute different values of k (number of k cluster equal to three had the greatest average silhouette width). The analysis was carried with the Free Statistic Software (ClustVis: a web tool for visualizing clustering of multivariate data (BETA), URL https://biit.cs.ut.ee/clustvis/)

Data Analysis and Statistics

Data were analyzed with Clampfit 10.6 (Molecular Devices) and Prism 6.0 (GraphPad, La Jolla, CA, USA). The AP train was generated by 1s current injection (with +20 pA increment for each step). The holding potential was approximately -65 mV. The R_{in} was defined by the ratio of steady-state voltage change of hyperpolarizing current (-10 pA, 1s). The membrane time constant (τ_m) was measured by using a single-exponential fit to the early portion of the voltage change produced by hyperpolarizing (-5 pA) current injection.

The threshold of AP was measured as the voltage at which the first derivative of

voltage exceeded 20 V/s (Hosp et al., 2014; Hou et al., 2016). The half-width of AP was measured at the two points during the rise and decay phase halfway between the threshold and peak. The AHP amplitude was defined as the most negative deflection following the peak of AP relative to the threshold. The max rising rate, the max falling rate and the peak amplitude were also calculated from the timing of AP threshold to AHP peak, using the AP evoked by the rheobase current (the minimal intensity of 1s current pulse required for AP generation) injection. The adaptation (AD) ratio is defined as the peak amplitude of the last spike divided by the first spike. The AD ratio, the coefficient of variation (CV) of inter- (ISI), the last spike onset, and the mean discharge frequency were measured during 1-s current step (100 pA) injection.

Two-tailed Fisher's exact test was used for statistical comparison of the connectivity in optogenetic-assisted mapping. Data were presented as mean ± standard error of mean (SEM). Error bars represent SEM. Statistical significance was tested by the Kruskal-Wallis ANOVA, Mann-Whitney t-test, Fisher's exact test and Pearson's normality test at the significance level (P) as indicated using Prism 6.0.

RESULTS

Distribution Patterns and Neurochemical Properties of VIP Neurons in the Brain

Identification of brain cell types is fundamental in modern neuroscience research. In addition to electrophysiological and anatomical properties, expression of specific molecular markers has been an important feature for defining a neuronal type. To date the advent of mouse genetics enables selective expression of fluorescent proteins or Cre recombinase in neurons with a specific molecular marker. Using these mouse lines as a tool, scientists are able to visualize neurons of a certain type and study their development, migration, distribution and connectivity across the mouse brain (Taniguchi et al., 2011; Pfeffer et al., 2013). To investigate the role of VIP INs in the DG circuitry, we took advantage of a VIP-ires-Cre knock-in mouse line by breeding with a Cre-dependent tdTomato reporter mouse Ai14 (Madisen et al., 2010; Taniguchi et al., 2011) (Figure 1*A*). This strategy enabled tdTomato expression in VIP-expressing cells in their offspring (i.e. *VIP-ires-Cre::Ai14*; Figure 1*A*). To observe the distribution of the VIP neurons, we performed serial coronal sections (60 μm per section) from the rostral to caudal part of the mouse brain (Figure 1*B*; age around 1-2 months). The tdTomato signal was detected in several brain areas (Figure 1*C*), including the neocortex (Figure 1*D*), hippocampus (Figure 1*D*), ventral suprachiasmatic nucleus (SCN; Figure 1*E*) and amygdala (Figure 1*F*). In the neocortex, tdTomato^{+} neurons were observed across layer II to VI, with a preferential distribution in superficial layers II-III (Figure 1*D*). In the hippocampal CA1 and DG, VIP neuron axons appeared in the stratum alveus (s.a), stratum pyramidale (s.p), stratum lacunosum-moleculare (s.lm) and hilus (h). Notably, approximately 10-15% of tdTomato^{+} cells in the DG resembled GCs (arrowheads in Figure 1*D*). In the amygdala,

tdTomato$^+$ neurons were mainly distributed in the basolateral amygdala (BLA), whereas tdTomato$^+$ axons were segregated in the central amygdala (CeA; Figure 1*F*).

In the sagittal sections, tdTomato$^+$ cells were observed in cortical and subcortical structures (Figure 2*A* and 2*B*). Similar to coronal sections, distribution patterns of tdTomato$^+$ cells were detected in the cortex and hippocampus (Figure 2*C* and 2*D*) and few of tdTomato$^+$ cells display GC-like morphology (Figure 2*D*; Arrowhead). Additionally, strong tdTomato expression was detected in the pontine reticular nucleus (PRNc; Figure 2*E*), inferior colliculus (IC; Figure 2*F*), retrosplenial area (RSP; Figure 2*F*), and outer layers of main olfactory bulb (MOB; Figure 2*G*). In a subset of experiments using transverse sections, the expression patterns of tdTomato$^+$ cells were also examined along the dorso-ventral axis (Figure 3). Note that strong tdTomato expression was detected in the subiculum (sub, Figure 3B_3-D_3). GC-like neurons were also identified in transverse sections of the DG (Figure 3B_3 and 3C_3; Arrowheads)

Comparison of Neurochemical Markers of VIP INs in the CA1 area and DG

To detect VIP expression in tdTomato$^+$ cells, we performed VIP immunohistochemistry (IHC) from *VIP-ires-Cre::Ai14* mouse brains (Figure 4A_1 and 4*A2*). Our results showed that 94.8 ± 1.3% of tdTomato$^+$ cells in the CA1 (n =20 slices from 2 mice; Figure 4B_1) and 81 ± 5% of tdTomato$^+$ cells in the DG (n =18 slices from 2 mice; Figure 4B_2) are VIP immunoreactive. Conversely, 92.8 ± 1.7% of VIP-immunoreactive cells in the CA1 (n =18 slices from 2 mice; Figure 4B_1) and 87.4 ± 3.1% of VIP-immunoreactive cells in the DG (n =18 slices from 2 mice; Figure 4B_2) are tdTomato$^+$ cells. Intriguingly, the VIP immunoreactivity of tdTomato$^+$ GC-like cells was negative (0/14 cells, n=18 slices from 2 mice), suggesting that VIP is preferentially expressed in non-GC cells (68/71 cells, n=18 from 2 mice). Taken together, the specificity and sensitivity of this mouse line for labeling

of VIP INs is reliable in the both CA1 and DG.

Some VIP INs in the neocortical and hippocampal CA1 areas co-express CCK or CR but not SST or PV (Taniguchi et al., 2011; Pfeffer et al., 2013; Tyan et al., 2014; Prönneke et al., 2015; Wall et al., 2016). To compare the neurochemical profiles of VIP INs in the DG with those in the CA1, we characterized VIP INs with antibodies against different neurochemical markers (Table 1 and table 2). Interneuron-selective (IS)-cells were identified based on expression of neurochemical markers such as CR or VIP in the hippocampus (Gulyás et al., 1996; Tyan et al., 2014). Colocalization of these two markers was detected in the neocortex and hippocampal CA1 (Acsády et al., 1996; Lee et al., 2010; Tyan et al., 2014). Consistently, approximately 30% of the VIP INs expressed CR in the CA1 (31.7 ± 5.8%, n = 14 slices from 3 mice, figure 4C_1). In contrast, only 17% of VIP INs in the DG expressed CR (17.6 ± 2.5%, n=25 slices from 3 mice, figure 4C_2). Additionally, previous studies demonstrated that VIP INs co-expressed CCK and displayed BC-like morphology, thereby providing perisomatic inhibition onto principal neurons (Hájos et al., 1996; Tyan et al., 2014). However, only few of VIP INs (6 ± 2.4%, n = 30 slices from 3 mice, figure 4*D1*) in the DG co-expressed CCK. This is in great contrast to the CA1 (27.7 ± 4.2%, n =11 slices from 2 mice, figure 4*D2*). In the DG, CCK^+ and PV^+ INs are two distinct populations and innervate the proximal dendrites or perisomatic domains of the GCs (Hefft and Jonas, 2005). We accordingly examined whether VIP INs expressed PV. We found no overlap between PV^+ cells and VIP cells in the both CA1 (0%, n=9 slices from 2 mice, figure 4E_1) and DG (0%, n = 14 slices from 2 mice, figure 4E_2). Finally, SST^+ and PV^+ INs are medial ganglionic eminence (MGE)-derived cells and substantially showed non-overlapping with caudal ganglionic eminence (CGE)-derived VIP INs (Rudy et al., 2011; Pfeffer et al., 2013). We finally

examined the immunoreactivity of SST in VIP INs. Our results showed no overlap between SST^+ cells and VIP cells both in the CA1 (0%, n = 9 slices from 2 mice, figure 4F_1) and DG (0%, n = 7 slices from 2 mice, figure 4F_2)

Morpho-physiological Differences Between tdTomato$^+$ GCs and INs

Our IHC results (Figure 4B_2) showed that approximately 10-15% of tdTomato$^+$ cells were VIP immunonegative and displayed GC-like morphology. However, it is difficult to distinguish those tdTomato$^+$ GC-like cells from VIP INs under epifluorescence microscope. To examine whether tdTomato$^+$ GC-like cells are functionally distinct from VIP INs, we characterized electrophysiological properties of all recorded tdTomato$^+$ cells. We randomly performed whole-cell patch-clamp recording from a sample of 122 tdTomato$^+$ cells in transverse hippocampal slices under IR-DIC and epifluorescent microscope (Figure 5*A*). Hyperpolarizing and depolarizing current steps (1s) were applied to assess their passive and active membrane properties. Biocytin was added in the recording pipette for subsequent *post hoc* morphological reconstruction. Anatomically, tdTomato$^+$ INs (termed VIP INs in the following experiments) displayed more branched dendrites and axonal arborization compared to tdTomato$^+$ GCs (Figure 5*B-F*). Electrophysiologically, VIP INs showed an obviously depolarized RMP (INs: -47.6 ± 1 mV, n = 106 vs. GCs: -77.1 ± 1.7 mV, n = 16; $p < 0.001$; Mann-Whitney unpaired t-test), smaller rheobase (INs: 16 ± 1.1 pA vs. GCs: 34.8 ± 4.5 pA; $p < 0.001$; Mann-Whitney unpaired t-test), larger R_{in} (INs: 915 ± 37.3 MΩ vs. GCs: 503.5 ± 53 MΩ; $p < 0.001$; Mann-Whitney unpaired t-test) compared to tdTomato$^+$ GCs. Furthermore, GCs exhibited stronger spike adaptation in response to current injection (Figure 5*B-G* and table 3). The scatter-plot of adaptation (AD) ratio versus RMP revealed two almost non-overlapping clusters (Figure 5*H*). Cell type identification based on single spike properties can give

rise to neuronal classification both *in vivo* and *ex vivo* (Henze et al., 2002; Hosp et al., 2014). Notably, half-width of single APs of tdTomato$^+$ INs was narrower than that of tdTomato$^+$ GCs (INs: 0.79 ± 0.02 ms vs. GCs: 1.02 ± 0.05 ms; $p < 0.001$; Mann-Whitney unpaired t-test). Additionally, VIP INs showed larger AHP (INs: -17.6 ± 0.4 mV vs. GCs: -13.7 ± 0.6 mV; $p < 0.001$; Mann-Whitney unpaired t-test), smaller AP peak amplitude (INs: 56.6 ± 1.1 mV vs. GCs: 91 ± 3.3 mV; $p < 0.001$; Mann-Whitney unpaired t-test), faster falling rate (INs: 126.4 ± 4.6 V/s vs. GCs: 89.1 ± 5.5 V/s; $p < 0.001$; Mann-Whitney unpaired t-test) compared to tdTomato$^+$ GCs (Figure 5*I*, 5*J* and table 3). In the following studies, we characterized putative VIP GABAergic INs based on the above morpho-eletrophysiological criteria.

Anatomical Diversity of the DG VIP INs

Based on the *post hoc* morphological reconstructions, VIP INs displayed heterogeneous axonal distribution patterns. According to the layer of axonal distribution, we classified VIP cells into four subtypes including hilus-projecting (HP) cells (27/40 cells), ML-projecting (MP) cells (6/40 cells), bistratified (Bis) cells (4/40 cells), and trilaminar (Tri) cells (3/40 cells) (Figure 6*A* and table 4). The axonal clusters of HP cells primarily arborized like ramified meshwork in the hilus. MP cells mostly distributed their axon in the IML and MML. Bis cells had unique axonal patterns, with two axonal collaterals located in the IML and hilus. The axons of Tri cells branched across three layers, and usually extended shortly after the origins. In terms of the dendritic pattern, most of the VIP INs dispersed their dendrites along the hilus-ML axis. Interestingly, 4 of 27 HP cells, 2 of 6 MP cells, 4 of 4 Bis cells and 0 of 3 Tri cells extended their dendrites to the subiculum (Supplementary figure 1). Finally, the somatic location of these four subtypes of VIP INs was also quite different. HP cells were largely located in the hilus whereas

other VIP IN subtypes were exclusively or primarily located in the ML (Figure 6*B* and supplementary figure 1).

Clustering Analysis of VIP INs Based on Electrophysiological Properties

Previous studies reported that VIP INs in the cortical area were likely composed of more diverse populations compared to other genetically-defined GABAergic INs (Prönneke et al., 2015; Wall et al., 2016). To classify the functional types of VIP INs, we performed the unbiased hierarchical clustering analysis (HCA) (Hosp et al., 2014; Hou et al., 2016). In order to validate each variable used in the clustering analysis, variables were examined by the normality and correlation tests (Supplementary figure 2 and table 5). The results were represented by the dendrogram and heatmap, in which three main classes of VIP INs can be identified based on passive and active membrane properties (Figure 7*A* and table 6). Class A VIP INs (n = 50) were characterized by rapidly adapting discharge activity (AD ratio; 0.13 ± 0.01) during depolarizing step current injection. Class B VIP INs (n = 15) were characterized by higher maximal firing frequency (57.7 ± 8.6 Hz) and larger Rin (1442 ± 80.9 MΩ) than remaining cells in the class A and C VIP INs. Class C VIP INs (n = 41) showed relatively large rheobase (22.7 ± 2 pA), small AHP (-16.5 ± 0.7 mV), hyperpolarizing RMP (-51.6 ± 1.5 mV) and irregular spiking properties which reflected on high CV of ISI (0.82 ± 0.09, Figure 8*B*).

Morpho-Physiological Criteria of VIP INs

VIP INs exhibited variable discharge patterns in response to 1-s depolarizing current steps injection. We arbitrarily divided them into three subtypes, so-called fast-adapting (FAD), regular spike (RS) and irregular spike (IRS; figure 8*A* and 8*B*). In 106 recorded cells, VIP INs predominantly exhibited FAD firing pattern (50/106 of total cells, figure 8*C*). We

finally correlated VIP subtypes defined by different approaches and found that class A, B and C VIP INs were mainly FAD, RS and IRS, respectively (Figure 8*D*). Notably, we observed that HP VIP INs exhibit faster and stronger spike adaptation compared to Bis VIP INs (Figure 8*E* and table 7). Moreover, MP VIP INs mostly showed irregular discharge activity compared to HP VIP INs (Figure 8*E* and table 7).

Late Recruitment of VIP INs by Cortical Excitatory Afferents

Dentate neurons receive coherent theta (4-10 Hz)-band excitatory inputs *in vivo*, predominantly relayed from the EC (Pernia-Andrade and Jonas, 2014). To assess the recruitment of VIP INs in response to successive PP inputs, we stimulated the cortical inputs, the medial and lateral PPs, by placing a stimulation electrode on the subiculum of the hippocampal fissure. While stimulating, we detected the action currents ('spikes') from individual VIP INs under cell-attached configuration (Figure 9*A*). To mimic the physiological condition, the trains of ten electrical stimuli were delivered at 10 Hz to the PP. Notably, most of the VIP INs did not respond to the initial stimuli but increased their firing probability to late stimuli during train stimulation (Figure 9*B* and 9*C*).

To probe this late-onset of VIP INs in response to cortical theta inputs, we compared the synaptic inhibitory drive across different levels of excitatory drive by converting inhibitory and excitatory synaptic currents to conductances (i.e., IPSG vs. EPSG). To isolate IPSG, we used a cesium-based internal pipette solution under voltage-clamp mode while recording at the AMPA receptor reversal potential (0 mV). In contrast, EPSGs were recorded at GABA receptor reversal potential (-50 mV). The depression of IPSG but facilitation of EPSG resulted in decreasing of I/E ratio (Figure 9*D-F*). In brief, late-recruitment of PP-VIP synapse may cause by short-term dynamic changed during theta cortical inputs.

VIP INs Preferentially Innervate INs in the DG

To understand the local connectivity between VIP INs and other neurons in the DG, we attempted to simultaneously record VIP INs and other neuronal types using pair recording (Figure 11). Surprisingly, we obtained a pair recording from VIP to VIP INs (Figure 10*A*). The presynaptic VIP IN is classified as Tri with the IRS pattern whereas the postsynaptic VIP IN is a MP cell with the FAD pattern (Figure 10*A*). On average, the first unitary Inhibitory postsynaptic current ($uIPSC_1$) was about 32.9 ± 7.2 pA (average of 7 trials). Notably, there is no reciprocal connections and gap junctions between these two cells. Additionally, a TML-like cell formed synapses with a FAD-HP-VIP IN (Figure 10*B*, $uIPSC_1$: 132.1 ± 10 pA, average of 40 trials). Our data indicated that VIP INs showed low connection probability with other neurons in the DG (Figure 10*C*, VIP IN-VIP IN: 1/29 cells, VIP IN-non VIP IN: 0/23, non VIP IN-VIP IN:1/23, VIP IN-MC: 0/2; MC-VIP IN: 0/2, VIP IN-GC: 0/3; GC-VIP IN: 0/3).

To assay inputs from broader populations of VIP INs, we alternatively utilized optogenetic stimulation to activate VIP INs and recorded postsynaptic GABAergic currents. We expressed the light-sensitive cation channel channelrhodopsin 2 (ChR2) in the dorsal or ventral DG of VIP-ires-Cre mice using viral injection. Adeno-associated virus (AAV) directed the expression of ChR2 following Cre-mediated recombination (Figure 11*A*). We found that ChR2-eYFP signal predominantly segregated in the hilus (Figure 11*B*), which was consistent with our previous tdTomato expression patterns. In whole-cell recording, the $eYFP^+$ cells generated inward depolarizing currents and APs in response to a train of 5-Hz short light pulses (5-ms in each pulse-width, Figure 11*C*, top). Similar responses were observed in response to a 500-ms sustained light pulse (Figure 11*C*, bottom). The photo-currents were recorded in all $eYFP^+$ INs in the presence of 1 μM

TTX, which blocked synaptic inputs and fast Na^+ channels (INs: 256.2 ± 33.6 pA, n = 8, successful rate: 8/8 v.s GCs: 46.4 ± 33.6 pA, n = 10, successful rate: 2/10). However, light-evoked responses were only detected in 2 out of 8 $eYFP^+$ GCs (Figure 11*D*) under the same conditions. To isolate VIP IN-mediated inhibitory transmission, a glutamatergic receptor blocker, kynurenic acid (2 mM) was bath applied in optogenetic-assisted mapping experiments.

To examined the functional connectivity of VIP INs, we recorded the IPSCs from different cell types in the DG (recorded currents were transformed to conductance in the following descriptions). Based on their morphological features, 6 different GABAergic INs subtypes and 2 glutamatergic neuronal subtypes were classified (Figure 12*A* and 12*B*). BC-like INs were identified by their axonal arborization, which are largely restricted in the GCL (IPSG1: 1.4 nS, 2/2 cells). The axonal arborization of HICAP-like cells was mainly confined to the IML (0.6 ± 0.2 nS, 10/13 cells). HIPP-like cells projected their axons mainly to the OML (0.2 nS, 5/7 cells), whereas TML-like cells spread their axons throughout the ML (0.3 nS, 1/1 cell). Hilar-INs were identified by their somata and neurites mainly located in the hilus (0.4 ± 0.1 nS, 11/13 cells). ML INs can be subdivided into MOPP cells and NGFCs in accordance with their neurochemical, morphological and physiological properties (Armstrong et al., 2011; Lee et al., 2016). In our experiments, MOPP cells were identified by their more branching dendritic structure (1.4 ± 0.4 nS, 4/9 cells), whereas NGFCs displayed short dendritic tree and exhibited late firing pattern in response to suprathreshold current injection (0.5 ± 0.4 nS, 3/8 cells) (Figure 12*A*). For glutamatergic cells, mossy cells (MCs) were identified by the large somatic size and the presence of thorny excrescences (Scharfman and Myers, 2013; Figure 12*B*; 0.05 nS, 2/12 cells) whereas GCs were distinguished by their dendritic pattern, mossy fibers and

relatively hyperpolarizing RMP (Figure 12*B*, 0.3 ± 0.2 nS, 3/36 cells). Our results showed that VIP INs had obviously higher connectivity with INs than with glutamatergic cells (Figure 12*D*, filled bar, INs: 36/53 vs non-IN: 5/48; $p < 0.001$; Two-tailed Fisher's exact test). Additionally, the local synaptic strength from VIP INs to GCs was small as compared to PV^+ and SST^+ INs in the DG (Supplementary figure 5). In summary, our results suggested that VIP INs engage in a disinhibitory circuitry, which may affect the excitability of the DG.

DISCUSSION

To understand the diversity and function of VIP INs in the mouse DG, we characterized morphological, neurochemical and physiological properties of VIP INs. We show that VIP INs comprise at least four subtypes in accordance with their distinct axonal projection patterns. Unlike other local-circuit GABAergic INs, VIP INs preferentially innervate INs over GCs and MCs. Taken together, VIP INs are IN-selective cells, which consist of diverse subtypes.

A Reliable Cre-Driver Mouse Line for Studying VIP INs

Selective targeting or manipulation of the VIP INs was difficult due to the lack of transgenic approaches. Recently, an up-to-date Cre driver line for VIP was produced (Taniguchi et al., 2011), which allows us to investigate the functional role of VIP INs across the mouse brain. However, the specificity and sensitivity of this mouse line for VIP INs in the DG remains unclear.

To address this question, we firstly quantified the colocalization of Cre-driven tdTomato protein with VIP in the hippocampal CA1 and DG using IHC. We found a high degree of overlap between tdTomato^{+} and VIP immunoreactive cells in the CA1 (~90%) and in the DG (~80%). Interestingly, a small population of tdTomato^{+} GCs is detected in the DG. Notably, these GCs are not VIP immunoreactive. A similar finding was observed in the same mouse line while crossing with Ai9 reporter mice (Taniguchi et al., 2011). A possible explanation for this paradox is a small amount of VIP expression in a certain population of GCs during development. Efficient Cre/loxP–mediated recombination may account for strong tdTomato expression.

The expression of Cre in a small population of GCs in this Cre driver line is a potential drawback for optogenetic control of VIP INs. To circumvent this problem, intersectional strategies that combine two recombination approaches are accessible (Taniguchi et al., 2011; Fenno et al., 2014). For example, the Dlx5/6-Flp driver expresses the recombinase FLPe in the cortical GABAergic neurons (Miyoshi et al., 2010). Hence, the use of *VIP-ires-Cre::Dlx5/6-Flp* mouse line may allow specific mapping of VIP INs and selective control of VIP INs.

Unique Cellular Profiles of VIP INs in the Mouse DG

Approximately 20% of VIP INs are CCK immunoreactive in the rat DG. These VIP/CCK INs display BC-like morphology (Hájos et al., 1996). In contrast, we observed only few VIP INs with axonal plexus restricted in the GCL. Furthermore, VIP INs are mostly immuno-negative for CCK in the mouse DG. The species difference is likely to account for the discrepancy. Although VIP INs also display a rich diversity in terms of their discharge pattern, the majority of VIP INs (~45%) exhibit strong AP amplitude adaptation. Additionally, DG VIP INs showed several unique cellular properties, including (i) small soma size and most of them projecting their axon to the hilus; (ii) large Rin (~900 MΩ), and depolarized RMP (~-48 mV). In the cell-attached recording, some of the VIP INs showed spontaneous firing activity (personal observation). This may be partly because of their more depolarized RMP and high Rin. Collectively, our data provide a novel insight into hitherto an uncharacterized neuronal population in the mouse DG.

Correlation Between Neurochemically, Morphologically and Physiologically Defined Cell Types

The linkages between each cellular profiles of INs have been widely investigated in the DG (Martina et al., 1998; Lien et al., 2001; Hefft and Jonas, 2005; Armstrong et al., 2011; Hosp et al., 2014; Yu et al., 2015). Based on our results, those physiologically-defined VIP INs are not remarkably associated with their distinct axonal patterns, indicating that INs cannot be unequivocally classified based on electrophysiological or morphological properties. Nevertheless, correlations are shown to exist between these properties and the gene or neurochemical markers (Lien et al., 2002; Pfeffer et al., 2013; Mardinly et al., 2016). Our IHC results suggest that CR^+ VIP INs are mostly detected in the subgranular zone of the DG (Figure 4*C*$_2$). In agreement with figure 6*B*, CR^+ VIP INs are mostly HP (Supplementary figure 3*A* and 3*B*). Additionally, most CR^+ VIP cells possess FAD discharge pattern (Supplementary figure 3*B*). In our CR immunostaining, more abundant CR^+ cells were detected in the ventral hilus compared to the dorsal hilus. This observation is in agreement with previous studies (Liu et al., 1996; Scharfman and Myers, 2013). Because CR signal is not detected in dorsal MCs, intense CR expression in the dorsal IML is likely the longitudinal axonal projections from ventral MCs, which express CR.

Cholinergic Modulation of VIP INs

The hippocampus receives neuromodulatory inputs from acetylcholine, serotonin, norepinephrine, oxyctocin and dopamine systems (Umbriaco et al., 1995; Kulkarni et al., 2002; Tirko et al., 2018). Disruption of these modulation systems may impair the neural activity and result in neuropsychiatric disorders, such as depression and schizophrenia (Lisman and Grace, 2005; Medrihan et al., 2017). Cholinergic input is known to

depolarize $5HT_{3A}R$-expressing GABAergic INs (Lee et al., 2010). Consistently, we showed that puffing of carbachol, a cholinergic agonist, can evoke fast depolarization in the DG VIP INs (Supplementary figure 4*A* and 4*B*). These data suggest that DG VIP INs may receive cholinergic activation via ionotropic nicotinic receptors.

Potential Role of VIP INs in the DG Networks

INs receive multiple excitatory afferents from different brain regions and shape the temporal dynamics of the hippocampal network (Pouille and Scanziani, 2004; Liu et al., 2014; Hsu et al., 2016; Lee et al., 2016). Here we showed that VIP INs receive synaptic currents, which exhibit short-term facilitation of EPSCs, in response to theta or gamma cortical activity (Figure 9*D* and supplementary figure 5*C* and 5*D*). Furthermore, we detect robust temporal summation in response to 10 to 30 Hz PP stimulation (Supplementary figure 5*A* and 5*B*, bottom). It is interesting to note that slow membrane depolarization and late-persistent firing (Supplementary figure 5*A* and 5*B*) are observed in 3 out 12 cells. Such strong temporal summation suggests that VIP INs may provide durably long-lasting inhibition onto the target INs during cortico-hippocampal information flow.

A classical view is that most of the DG INs directly innervate GCs through the feedback and feedforward inhibition. However, little is known about the synaptic role of IN-selective INs in the DG microcircuit. Several studies have addressed the postsynaptic targets of VIP INs using paired recordings, optogenetic approaches or ultrastructural methods (Hájos et al., 1996; Lee et al., 2013; Pfeffer et al., 2013; Pi et al., 2013; Tyan et al., 2014). Those studies indicate that VIP INs preferentially regulate local circuits via disinhibition. In order to examine the cell-type specific projection from distinct classes of VIP INs, we performed paired-recording. Unfortunately, VIP INs form synapses with postsynaptic neurons with low connectivity. Alternatively, we used optogenetic approach

to address this question. Based on the result of optogenetic-assisted mapping, VIP INs rarely target glutamatergic cells (GCs and MCs) but specialized in innervating other INs. Compared with PV^+ and SST^+ INs, VIP INs innervate GCs with low connection probability and weak synaptic strength (Supplementary figure 5*G* and 5*H*).

The results of optogenetic-assisted mapping suggests that VIP INs preferentially control the excitability of other INs. Therefore, VIP INs are likely to regulate the dentate GCs via disinhibition. To examine the interaction between VIP INs and GCs, we optogenetically activated or silenced VIP cells (Figure 11 and supplementary figure 6), then monitored the population spike (pSpike) of GCs evoked by PP stimulation (Supplementary figure 7) (Lee et al., 2016). However, we did not detect the change of pSpike while manipulating the activity of VIP INs. It might because of VIP INs have low release probability or VIP INs control their downstream neurons with weak synaptic strength. Another possibility is that disinhibitory control of VIP INs cannot efficiently influence the GC excitability. Instead, VIP INs may regulate other synaptic function of GCs, such as long-terms plasticity.

Potential Roles of VIP INs in DG-dependent Cognition and Emotion

In cortical regions, VIP INs suppress the firing of other local INs during complex behaviors (Pi et al., 2013; Fu et al., 2014; Park et al., 2015; Jackson et al., 2016; Mardinly et al., 2016; Garcia-Junco-Clemente et al., 2017), including locomotion, visual processing and other sensory reinforcement. VIP INs are active when the mouse is whisking, whereas they are inactive during non-whisking periods, thereby providing an activity-dependent gain control of disinhibition (Lee et al., 2013). Similarly, VIP INs in the DG may control DG-dependent contextual learning or stress-related emotional behaviors (Kheirbek et al., 2013). Further experiments will be required to investigate the functional role of VIP INs

in freely-moving animals.

REFERENCES

Acsády L, Görcs TJ, Freund TF (1996) Different populations of vasoactive intestinal polypeptide-immunoreactive interneurons are specialized to control pyramidal cells or interneurons in the hippocampus. Neuroscience 73:317-334

Armstrong C, Szabadics J, Tamás G, Soltesz I (2011) Neurogliaform cells in the molecular layer of the dentate gyrus as feed-forward γ-aminobutyric acidergic modulators of entorhinal-hippocampal interplay. J Comp Neurol 519:1476-1491

Chiang PH, Wu PY, Kuo TW, Liu YC, Chan CF, Chien TC, Cheng JK, Huang YY, Chiu CD, Lien CC (2012) GABA is depolarizing in hippocampal dentate granule cells of the adolescent and adult rats. J Neurosci 32:62-67

Donato F, Rompani SB, Caroni P (2013) Parvalbumin-expressing basket-cell network plasticity induced by experience regulates adult learning. Nature 504:272-276

Ewell LA, Jones MV (2010) Frequency-tuned distribution of inhibition in the dentate gyrus. J Neurosci 30:12597-12607

Fanselow MS, Dong HW (2010) Are the dorsal and ventral hippocampus functionally distinct structures. Neuron 65:7-19

Fenno LE, Mattis J, Ramakrishnan C, Hyun M, Lee SY, He M, Tucciarone J, Selimbeyoglu A, Berndt A, Grosenick L, Zalocusky KA, Bernstein H, Swanson H, Perry C, Diester I, Boyce FM, Bass CE, Neve R, Huang ZJ, Deisseroth K (2014) Targeting cells with single vectors using multiple-feature Boolean logic. Nat Methods 11:763-772

Freund TF, Buzsáki G (1996) Interneurons of the hippocampus. Hippocampus 6:347-470

Fu Y, Tucciarone JM, Espinosa JS, Sheng N, Darcy DP, Nicoll RA, Huang ZJ, Stryker MP (2014) Cell 156:1139-1152.

Garcia-Junco-Clemente P, Ikrar T, Tring E, Xu X, Ringach DL, Trachtenberg JT (2017) An inhibitory pull-push circuit in frontal cortex. Nat Neurosci 20:389-392

Gidon A, Segev I (2012) Principles governing the operation of synaptic inhibition in dendrites. Neuron 75:330-341

Gulyás AI, Hájos N, Freund TF (1996) Interneurons containing calretinin are specialized to control other interneurons in the rat hippocampus. J Neurosci 16:3397-3411

Gupta A, Wang Y, Markram H (2000) Organizing principles for a diversity of GABAergic interneurons and synapses in the neocortex. Science 287:273-278

Hájos N, Acsady L, Freund TF (1996) Target selectivity and neurochemical characteristics of VIP-immunoreactive interneurons in the rat dentate gyrus. Eur J Neurosci 8:1415-1431

Halasy K, Somogyi P (1993) Subdivisions in the multiple GABAergic innervation of granule cells in the dentate gyrus of the rat hippocampus. Eur J Neurosci 5:411-429

Hefft S, Jonas P (2005) Asynchronous GABA release generates long lasting inhibition at a hippocampal interneuron-principal neuron synapse. Nat Neurosci 8:1319–1328

Henze DA, Wittner L, Buzsáki G (2002) Single granule cells reliably discharge targets in the hippocampal CA3 network in vivo. Nat Neurosci 5:790-795

Hosp JA, Strüber M, Yanagawa Y, Obata K, Vida I, Jonas P, Bartos M (2014) Morpho-physiological criteria divide dentate gyrus interneurons into classes. Hippocampus 24:189-203

Hou WH, Kuo N, Fang GW, Huang HS, Wu KP, Zimmer A, Cheng JK, Lien CC (2016) Wiring specificity and synaptic diversity in the mouse lateral central amygdala. J Neurosci 36:4549-4563

Hsu TT, Lee CT, Tai MH, Lien CC (2015) Differential recruitment of dentate gyrus interneuron types by commissural versus perforant pathways. Cereb Cortex 26:2715-2727

Hu H, Gan J, Jonas P (2014) Interneurons. Fast-spiking, parvalbumin^{+} GABAergic interneurons: from cellular design to microcircuit function. Science 345:1255263

Isaacson JS, Scanziani M (2011) How inhibition shapes cortical activity. Neuron 72:231-243.

Jackson J, Ayzenshtat I, Karnani MM, Yuste R. (2016) VIP^{+} interneurons control neocortical activity across brain states. J Neurophysiol 115:3008-3017.

Karnani MM, Jackson J, Ayzenshtat I, Hamzehei Sichani A, Manoocheri K, Kim S, Yuste R (2016) Opening holes in the blanket of inhibition: localized lateral disinhibition by VIP interneurons. J Neurosci 36:3471–3480

Kheirbek MA, Drew LJ, Burghardt NS, Costantini DO, Tannenholz L, Ahmari SE, Zeng H, Fenton AA, Hen R (2013) Differential control of learning and anxiety along the dorsoventral axis of the dentate gyrus. Neuron 77:955-968

Klausberger T, Somogyi P (2008) Neuronal diversity and temporal dynamics: the unity of hippocampal circuit operations. Science 321:53-57

Kohara K, Pignatelli M, Rivest AJ, Jung HY, Kitamura T, Suh J, Frank D, Kajikawa K, Mise N, Obata Y, Wickersham IR, Tonegawa S (2014) Cell type-specific genetic and

optogenetic tools reveal hippocampal CA2 circuits. Nat Neurosci 17:269-279

Krueppel R, Remy S, Beck H (2011) Dendritic integration in hippocampal dentate granule cells. Neuron 71:512–528

Kulkarni VA, Jha S, Vaidya VA (2002) Depletion of norepinephrine decreases the proliferation, but does not influence the survival and differentiation, of granule cell progenitors in the adult rat hippocampus. Eur J Neurosci 16:2008-2012

Lapray D, Lasztoczi B, Lagler M, Viney TJ, Katona L, Valenti O, Hartwich K, Borhegyi Z, Somogyi P, Klausberger T (2012) Behavior-dependent specialization of identified hippocampal interneurons. Nat Neurosci 15:1265-1271

Lee CT, Kao MH, Hou WH, Wei YT, Chen CL, Lien CC (2016) Causal evidence for the role of specific GABAergic interneuron types in entorhinal recruitment of dentate granule cells. Sci Rep 6:36885

Lee S, Hjerling-Leffler J, Zagha E, Fishell G, Rudy B (2010) The largest group of superficial neocortical GABAergic interneurons expresses ionotropic serotonin receptors. J Neurosci 30:16796-16808

Lee S, Kruglikov I, Huang ZJ, Fishell G, Rudy B (2013) A disinhibitory circuit mediates motor integration in the somatosensory cortex. Nat Neurosci 16:1662-1670

Leutgeb JK, Leutgeb S, Moser MB, Moser EI (2007) Pattern separation in the dentate gyrus and CA3 of the hippocampus. Science 315:961–966

Lien CC, Martina M, Schultz JH, Ehmke H, Jonas P (2002) Gating, modulation and subunit composition of voltage-gated K (+) channels in dendritic inhibitory interneurones of rat hippocampus. J Physiol 538:405-419

Lisman JE, Grace AA (2005) The hippocampal-VTA loop: controlling the entry of information into long-term memory. Neuron 46:703-713

Liu Y, Fujise N, Kosaka T (1996) Distribution of calretinin immunoreactivity in the mouse dentate gyrus. I. General description. Exp Brain Res 108:389-403

Liu YC, Cheng JK, Lien CC (2014) Rapid dynamic changes of dendritic inhibition in the dentate gyrus by presynaptic activity patterns. J Neurosci 34:1344–1357

Madisen L, Zwingman TA, Sunkin SM, Oh SW, Zariwala HA, Gu H, Ng LL, Palmiter RD, Hawrylycz MJ, Jones AR, Lein ES, Zeng H (2010) A robust and high-throughput Cre reporting and characterization system for the whole mouse brain. Nat Neurosci 13:133-140

Mardinly AR, Spiegel I, Patrizi A, Centofante E, Bazinet JE, Tzeng CP, Mandel-Brehm C, Harmin DA, Adesnik H, Fagiolini M, Greenberg ME (2016) Sensory experience regulates cortical inhibition by inducing IGF1 in VIP neurons. Nature 531:371-375.

Markram H, Toledo-Rodriguez M, Wang Y, Gupta A, Silberberg G, Wu C (2004) Interneurons of the neocortical inhibitory system. Nat Rev Neurosci 5:793-807.

Marlin BJ, Mitre M, D'amour JA, Chao MV, Froemke RC (2015) Oxytocin enables maternal behaviour by balancing cortical inhibition. Nature 520:499-504

Martina M, Schultz JH, Ehmke H, Monyer H, Jonas P. (1998) Functional and molecular differences between voltage-gated K+ channels of fast-spiking interneurons and pyramidal neurons of rat hippocampus. J Neurosci 18:8111-8125

McBain CJ, Fisahn A (2001) Interneurons unbound. Nat Rev Neurosci 2:11-23

Medrihan L, Sagi Y, Inde Z, Krupa O, Daniels C, Peyrache A, Greengard P (2017)

Initiation of behavioral response to antidepressants by cholecystokinin neurons of the dentate gyrus. Neuron 95:564-576

Miles R, Tóth K, Gulyás AI, Hájos N, Freund TF (1996) Differences between somatic and dendritic inhibition in the hippocampus. Neuron 16:815-823

Milner B (1968) Further analysis of the hippocampal amnesic syndrome: 14-year follow-up study of H.M. Neuropsychologia 6:215-234

Miyoshi G, Hjerling-Leffler J, Karayannis T, Sousa VH, Butt SJ, Battiste J, Johnson JE, Machold RP, Fishell G (2010) Genetic fate mapping reveals that the caudal ganglionic eminence produces a large and diverse population of superficial cortical interneurons. J Neurosci 30:1582-1594

Park SJ, Borghuis BG, Rahmani P, Zeng Q, Kim IJ, Demb JB (2015) Function and circuitry of VIP+ interneurons in the mouse retina. J Neurosci 35:10685-10700

Pernía-Andrade AJ, Jonas P (2014) Theta-gamma-modulated synaptic currents in hippocampal granule cells in vivo define a mechanism for network oscillations. Neuron 81:140-152

Petilla Interneuron Nomenclature Group, Ascoli GA, Alonso-Nanclares L, Anderson SA, Barrionuevo G, Benavides-Piccione R, Burkhalter A, Buzsáki G, Cauli B, Defelipe J, Fairén A, Feldmeyer D, Fishell G, Fregnac Y, Freund TF, Gardner D, Gardner EP, Goldberg JH, Helmstaedter M, Hestrin S, Karube F, Kisvárday ZF, Lambolez B, Lewis DA, Marin O, Markram H, Muñoz A, Packer A, Petersen CC, Rockland KS, Rossier J, Rudy B, Somogyi P, Staiger JF, Tamas G, Thomson AM, Toledo-Rodriguez M, Wang Y, West DC, Yuste R (2008) Petilla terminology: nomenclature of features of GABAergic interneurons of the cerebral cortex. Nat Rev Neurosci 9:557-568

Pfeffer CK (2014) Inhibitory neurons: vip cells hit the brake on inhibition. Curr Biol 24:18-20

Pfeffer CK, Xue M, He M, Huang ZJ, Scanziani M (2013) Inhibition of inhibition in visual cortex: the logic of connections between molecularly distinct interneurons. Nat Neuroscience 1068-1076.

Pi HJ, Hangya B, Kvitsiani D, Sanders JI, Huang ZJ, Kepecs A (2013) Cortical interneurons that specialize in disinhibitory control. Nature 503:521-524.

Pouille F, Scanziani M (2004) Routing of spike series by dynamic circuits in the hippocampus. Nature 429:717-723

Prönneke A, Scheuer B, Wagener RJ, Möck M, Witte M, Staiger JF (2015) Characterizing VIP neurons in the barrel cortex of VIPcre/tdTomato mice reveals layer-specific differences. Cereb Cortex 25:4854-4868.

Rizzo A, Carratelli CR, De Filippis A, Bevilacqua N, Tufano MA, Buommino E (2014) Transforming activities of Chlamydia pneumoniae in human mesothelial cells. Int Microbiol 17:185-193

Rousseeuw PJ (1987) Silhouettes: A graphical aid to the interpretation and validation of cluster analysis. J Comput Appl Math 20:53-65

Rudy B, Fishell G, Lee S, Hjerling-Leffler J (2011) Three groups of interneurons account for nearly 100% of neocortical GABAergic neurons. Dev Neurobiol 71:45-61.

Savanthrapadian S, Meyer T, Elgueta C, Booker SA, Vida I, Bartos M (2014) Synaptic properties of SOM- and CCK-expressing cells in dentate gyrus interneuron networks. J Neurosci 34:8197-8209.

Scharfman HE, Myers CE (2013) Hilar mossy cells of the dentate gyrus: a historical perspective. Front Neural Circuits 6:106.

Scoville WB, Milner B (1957) Loss of recent memory after bilateral hippocampal lesions. J Neurol Neurosurg Psychiatry 20:11-21

Taniguchi H, He M, Wu P, Kim S, Paik R, Sugino K, Kvitsiani D, Fu Y, Lu J, Lin Y, Miyoshi G, Shima Y, Fishell G, Nelson SB, Huang ZJ (2011) A resource of Cre driver lines for genetic targeting of GABAergic neurons in cerebral cortex. Neuron 71:995-1013

Tirko NN, Eyring KW, Carcea I, Mitre M, Chao MV, Froemke RC, Tsien RW (2018) Oxytocin transforms firing mode of CA2 hippocampal neurons. Neuron 30781-5

Tyan L, Chamberland S, Magnin E, Camiré O, Francavilla R, David LS, Deisseroth K, Topolnik L (2014) Dendritic inhibition provided by interneuron-specific cells controls the firing rate and timing of the hippocampal feedback inhibitory circuitry. J Neurosci 34:4534-4547.

Umbriaco D, Garcia S, Beaulieu C, Descarries L (1995) Relational features of acetylcholine, noradrenaline, serotonin and GABA axon terminals in the stratum radiatum of adult rat hippocampus. Hippocampus 5:605-620

Walker F, Möck M, Feyerabend M, Guy J, Wagener RJ, Schubert D, Staiger JF, Witte M (2016) Parvalbumin- and vasoactive intestinal polypeptide-expressing neocortical interneurons impose differential inhibition on Martinotti cells. Nat Commun 7:13664

Wall NR, De La Parra M, Sorokin JM, Taniguchi H, Huang ZJ, Callaway EM (2016) Brain-wide maps of synaptic input to cortical interneurons. J Neurosci 36:4000-4009

Ward, JH (1963) Hierarchical grouping to optimize an objective function. J Am Stat

Assoc 58:236-244

Yu J, Swietek B, Proddutur A, Santhakumar V (2015) Dentate total molecular layer interneurons mediate cannabinoid-sensitive inhibition. Hippocampus 25:884-889

FIGURES AND TABLES

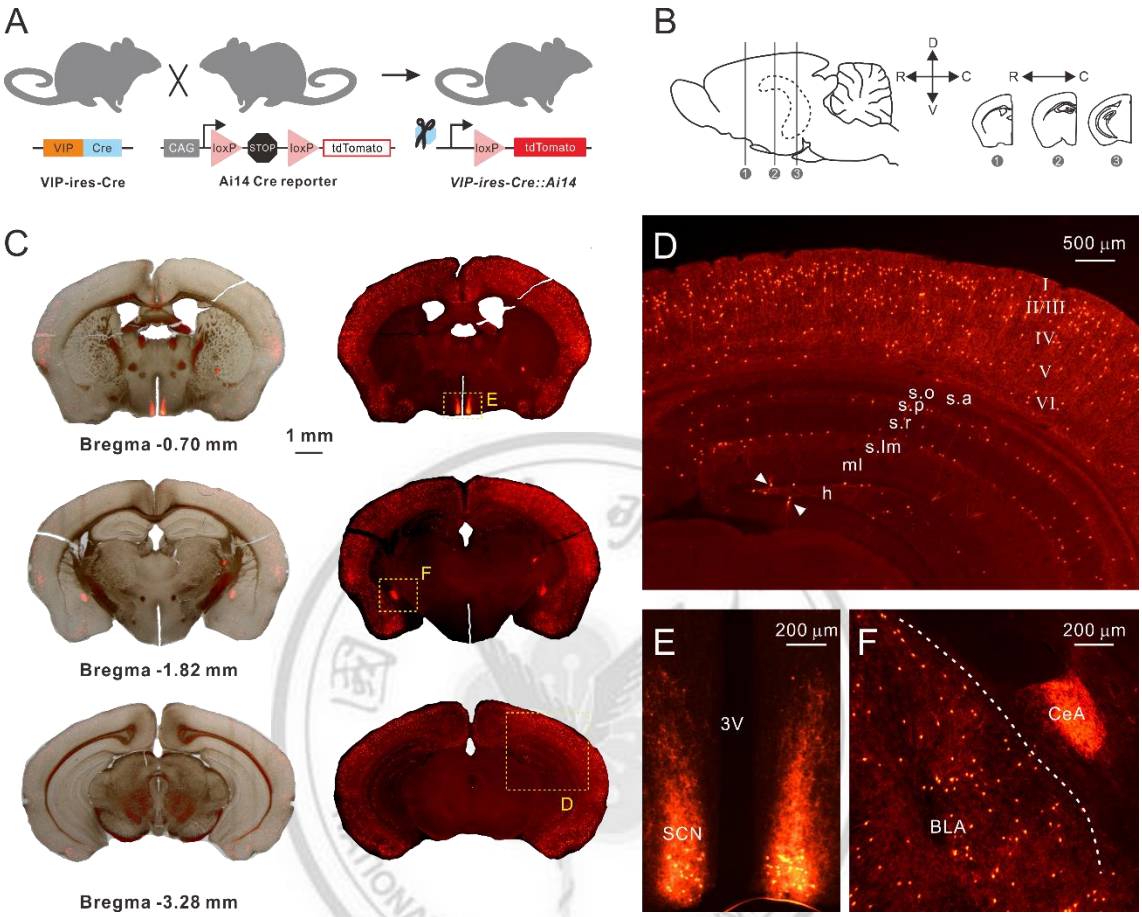

Figure 1. VIP-expressing cells in the brain of *VIP-ires-Cre::Ai14* mice

(A) The mating strategy of using VIP-ires-Cre and a reporter line to label VIP neurons. Ai14 Cre reporter mice harbor a loxP-flanked STOP cassette preventing transcription of the CAG promoter-driven tdTomato red fluorescent protein. The Cre recombinase ("scissor") excises the STOP codon and results in transcription of tdTomato in *VIP-ires-Cre::Ai14* mice.

(B) Left, diagram of a lateral view of mouse brain. Straight lines indicated the coronal section cut through one hemisphere which contained the hippocampus (dotted line). D, dorsal; V, ventral; R, rostral; C, caudal. Right, three coronal sections from the rostral to

caudal part

(C) Left, overlay of bright-field and epifluorescence images from the brain sections as indicated in (B, right). Right, epifluorescence images; the enlarged images of the yellow boxes were shown in D, E and F.

(D) Distribution of VIP neurons in an adult *VIP-ires-Cre::Ai14* mouse cortex and hippocampus. Note the neurites of VIP neurons segregated into distinct laminae in the stratum oriens (s.o), stratum pyramidale (s.p) and hilus (h). The arrowheads indicated the GC-like neurons. s.r, stratum radiatum; s.lm, stratum lacunosum moleculare; ml, molecular layer.

(E) A higher magnification of suprachiasmatic nucleus (SCN). Note the dense VIP cell bodies located in the ventral SCN.

(F) A higher magnification of central amygdala (CeA) and basolateral amygdala (BLA). Note the dense neurites segregated into the CeA.

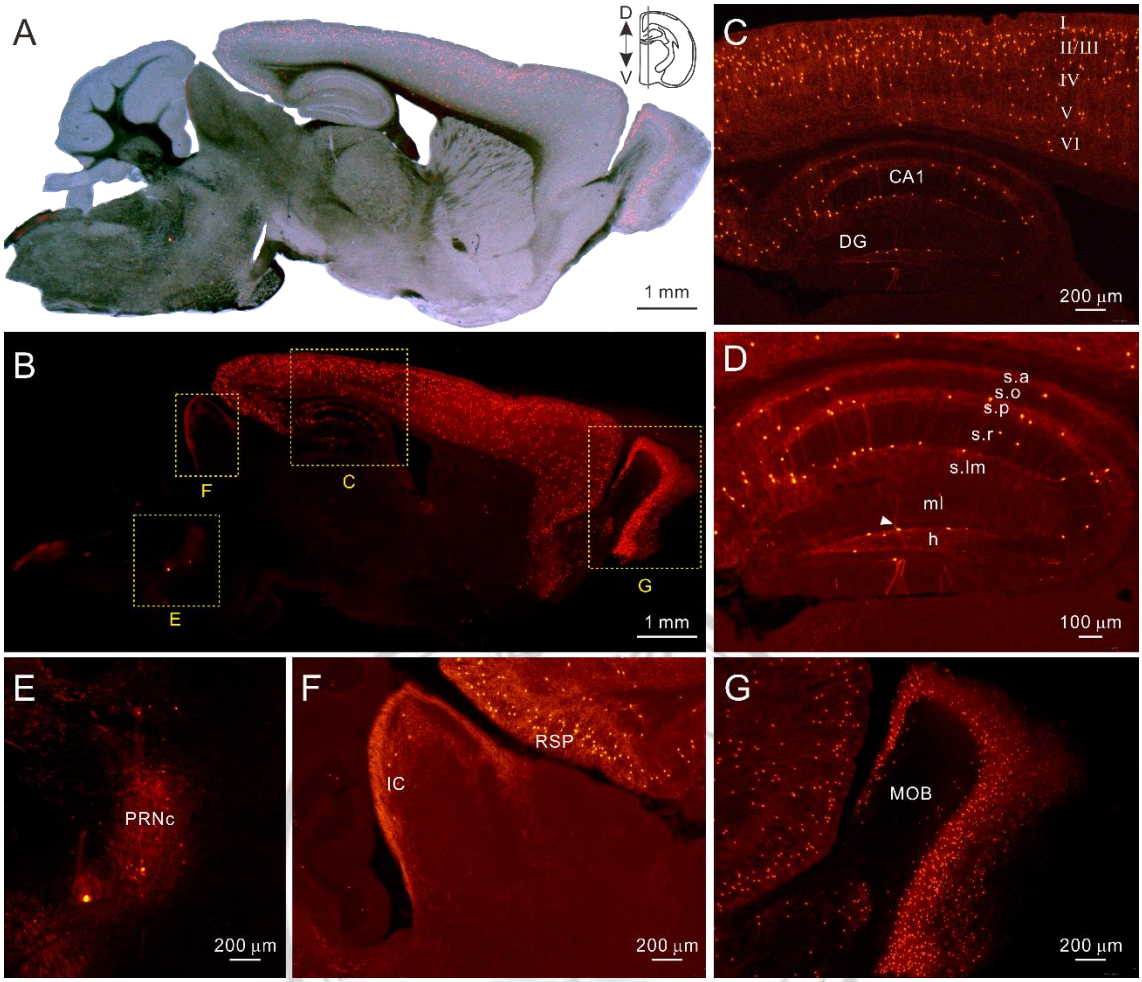

Figure 2. The sagittal sections of the brain from *VIP-ires-Cre::Ai14* mice

(A and B) A, overlay of bright-field and epifluorescence images. Panel, the straight line indicated the parasagittal section plane. B, epifluorescence image; the enlarged images of the yellow boxes were shown in *C, E, F and G.*

(C and D) Distribution of VIP neurons in an adult *VIP-ires-Cre::Ai14* mouse cortex and hippocampus. The arrowheads indicated the GC-like neuron.

(E-G) Dense signals were detected in the pontine reticular nucleus (PRNc), inferior colliculus (IC), retrosplenial area (RSP) and main olfactory bulb (MOB).

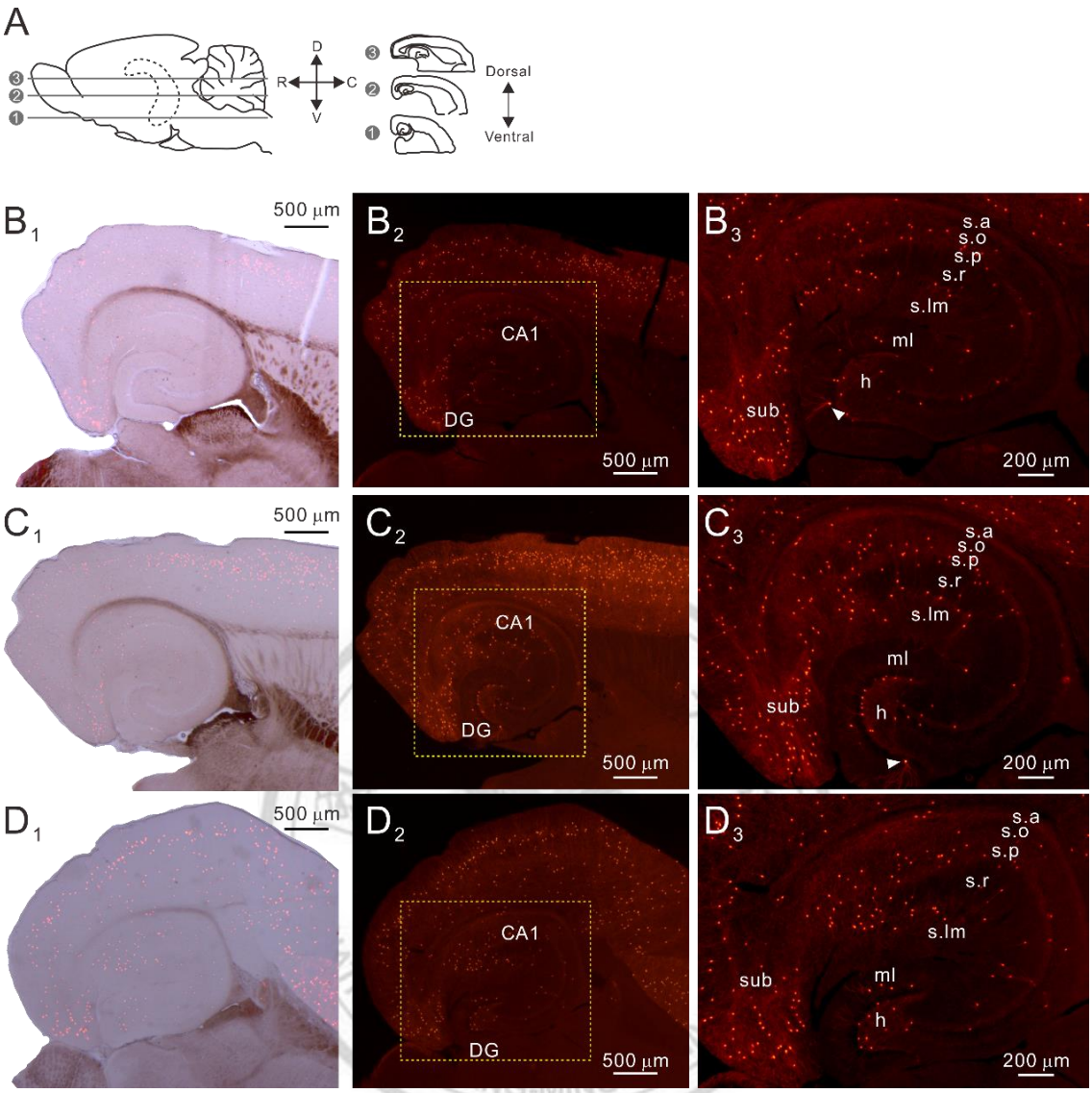

Figure 3. The transverse sections of the brain from *VIP-ires-Cre::Ai14* mice

(A) Diagram of the orientation for transverse sections from the dorsal to ventral axis.

(B_1, C_1 and D_1) Overlay of bright-field and epifluorescence images from the brain sections as indicated in *A*.

(B_2, C_2 and D_2) Epifluorescence images; the enlarged images of the yellow boxes were shown in *B_3, C_3 and D_3*.

(B_3, C_3 and D_3) Transverse section of the hippocampal CA and DG. Note the abundance

cell bodies were detected in the subiculum (sub). The arrowheads indicated the GC-like neurons.

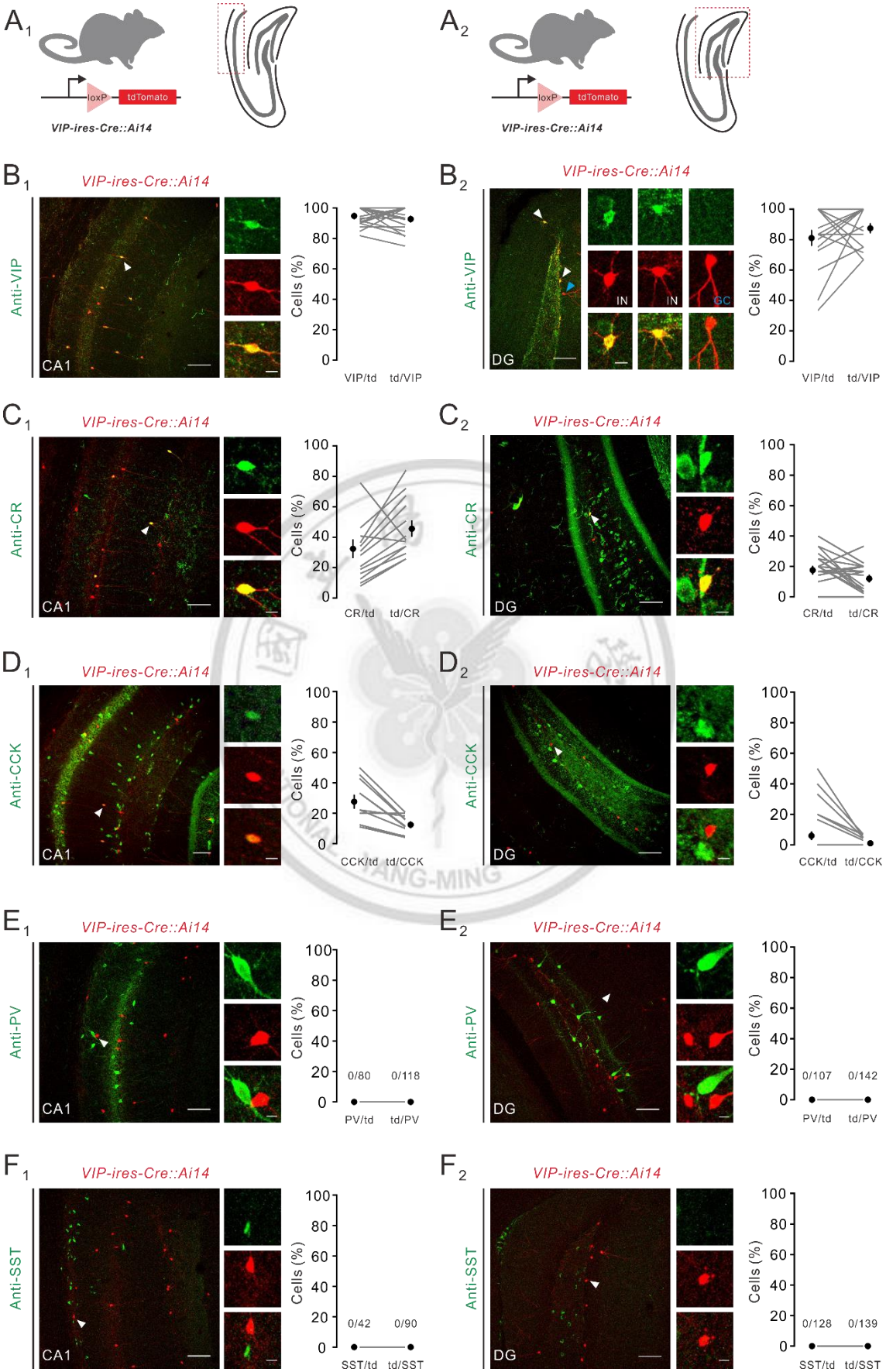
A1
loxP
tdTomato
VIP-ires-Cre::Ai14
A2
loxP
tdTomato
VIP-ires-Cre::Ai14
B1
VIP-ires-Cre::Ai14
Anti-VIP
CA1
Cells (%)
VIP/td td/VIP
B2
VIP-ires-Cre::Ai14
Anti-VIP
DG
IN
IN
GC
Cells (%)
VIP/td td/VIP
C1
VIP-ires-Cre::Ai14
Anti-CR
CA1
Cells (%)
CR/td td/CR
C2
VIP-ires-Cre::Ai14
Anti-CR
DG
Cells (%)
CR/td td/CR
D1
VIP-ires-Cre::Ai14
Anti-CCK
CA1
Cells (%)
CCK/td td/CCK
D2
VIP-ires-Cre::Ai14
Anti-CCK
DG
Cells (%)
CCK/td td/CCK
E1
VIP-ires-Cre::Ai14
Anti-PV
CA1
Cells (%)
0/80 0/118
PV/td td/PV
E2
VIP-ires-Cre::Ai14
Anti-PV
DG
Cells (%)
0/107 0/142
PV/td td/PV
F1
VIP-ires-Cre::Ai14
Anti-SST
CA1
Cells (%)
0/42 0/90
SST/td td/SST
F2
VIP-ires-Cre::Ai14
Anti-SST
DG
Cells (%)
0/128 0/139
SST/td td/SST

Figure 4. Neurochemical properties of VIP neurons in the DG and CA1 areas

(A_1 and *B_1)* IHC stainings were performed with coronal sections of *VIP-ires-Cre::Ai14*. The box indicated the CA1 and DG areas for the analysis of immunochemical markers.

(B-F) Confocal images stacks illustrated the immunoreactivity of VIP, CR, CCK, PV and SST in the hippocampal CA1 and DG. The arrowheads were shown at a higher magnification in the inset. Closed circles were the average of the colocalizations. Connected lines indicated the quantifications from same vision. Scale bar: 100 µm; Scale bar for enlarged cells in the inset: 10 µm. Data were expressed as mean ± SEM.

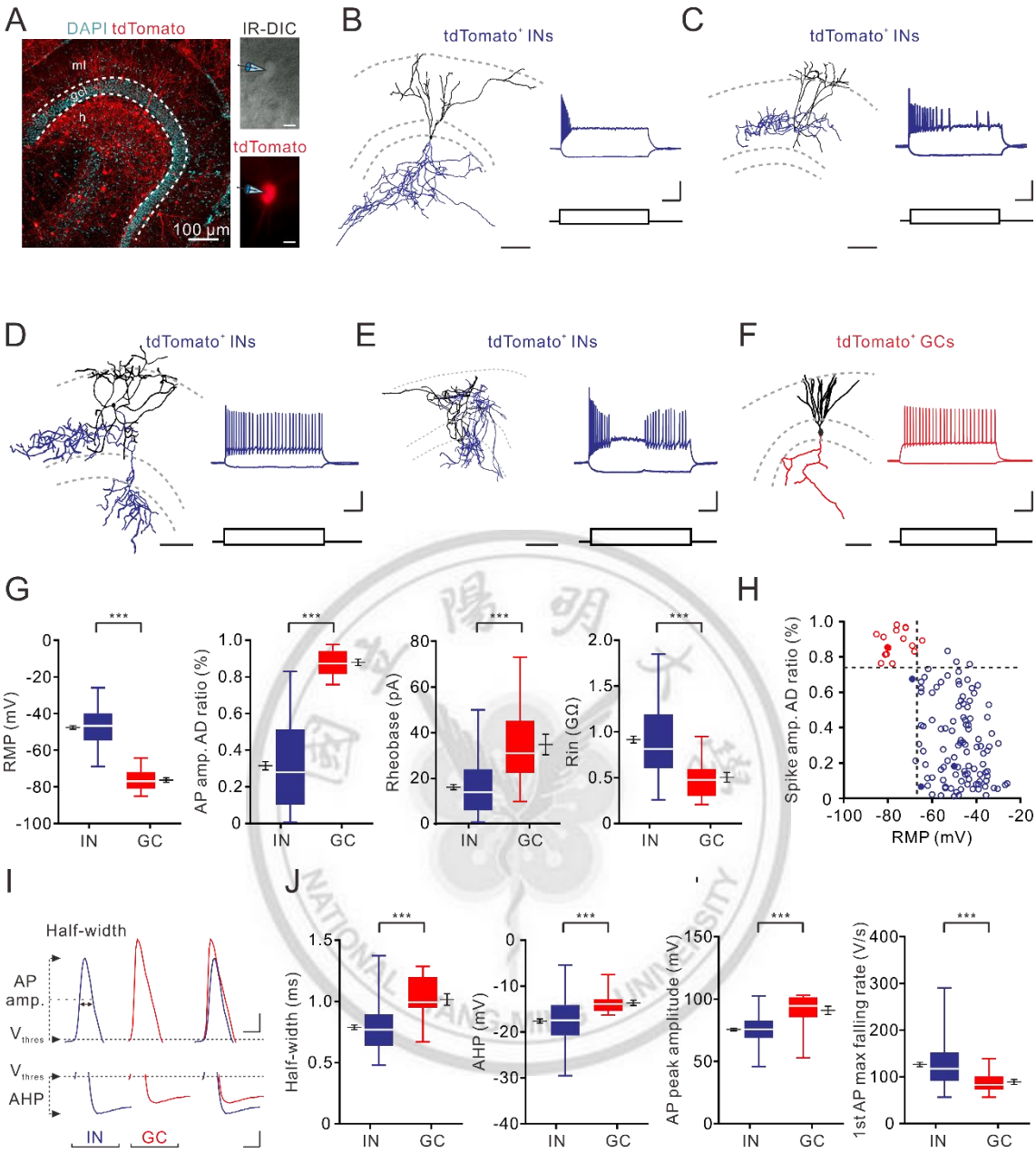

Figure 5. Distinct morphological patterns and electrophysiological characteristics of tdTomato-expressing neurons

(A) Left, Two-photon image stacks of tdTomato and DAPI signals in the DG. A transverse hippocampal section was taken from a *VIP-ires-Cre::Ai14* mouse. Right, IR-DIC (top) and the tdTomato fluorescence (bottom) images. A schematic recording pipette was attached to the recorded cell.

(B-F) The morphologies and discharge patterns of tdTomato$^+$ neurons. Somata and dendrites of INs were in black and the axons were in blue; the soma and dendrites of GC were in black and the axons were in red. Scale bars: 40 mV, 100 pA, 200 ms, 100 μm.

(G) Whisker plots showed differences of intrinsic properties between tdTomato$^+$ INs (n=106) and tdTomato$^+$ GCs (n=16). Mean ± SEM were represented close to the boxes. ***$p < 0.001$.

(H) Scatterplot of spike amplitude adaptation (AD) ratio versus RMP. Red and blue dots represented GCs and INs, respectively. Dashed lines indicate the arbitrary cutoff values (AD ratio of 0.75; RMP of -68 mV) that appropriately differentiate two populations. The filled circles represented the neurons shown in *B-F.*

(I) Representative traces of single APs in response to rheobase current injection recorded from tdTomato$^+$ INs and tdTomato$^+$ GCs. Upper traces represented the overshooting part of single spikes. Scale bar: 20 mV, 1 ms. Lower traces represented the AHP of the same spike. Scale bar: 10 mV, 0.5 ms.

(J) Comparison of single APs properties between tdTomato$^+$ INs and tdTomato$^+$ GCs. Mean ± SEM were represented close to the boxes. ***$p < 0.001$.

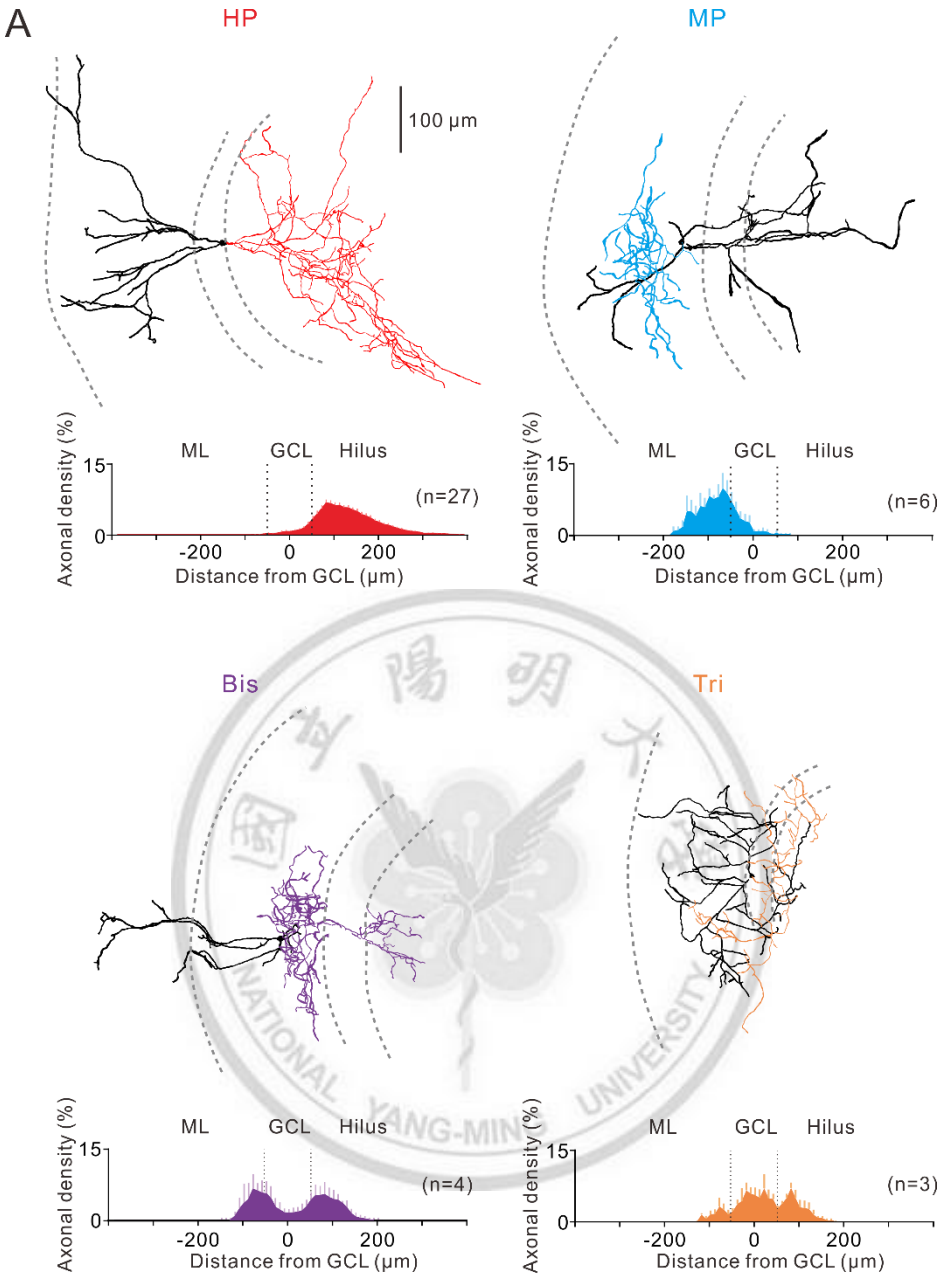
A
HP
MP
100 µm
ML
GCL
Hilus
Axonal density (%)
15
0
(n=27)
(n=6)
-200
0
200
Distance from GCL (µm)
Bis
Tri
(n=4)
(n=3)

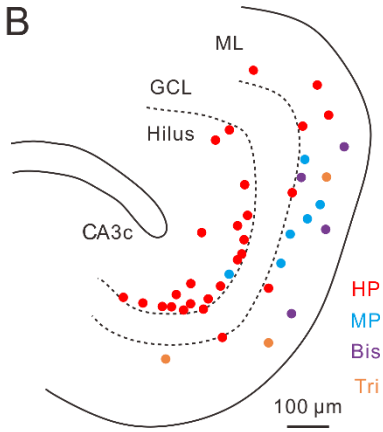
B
ML
GCL
Hilus
CA3c
HP
MP
Bis
Tri
100 µm

Figure 6. Axonal distributions of various VIP IN subtypes

(A) Top, exemplar reconstructions of a hilus-projecting cells (HP) with the axonal collateral project to the hilus; a ML-projecting cells (MP) with axonal distributions located in the IML and middle molecular layer (MML); a bistratified cells (Bis) with two clusters of axonal plexus distributed in the IML and hilus; a trilamilar cells (Tri) with axonal arborization distributed throughout three layers. Somata and dendrites were in black. Axons of HP, MP, Bis and Tri were in red, blue, purple and orange, respectively. Bottom, the normalized axonal density across different layers of the DG.

(B) Distribution of the 40 recorded cells. Note that the HP VIP cells were primarily located in the hilus (20/27 cells), whereas other VIP IN types were primarily or exclusively located in the ML (MP: 5/6 cells, Bis: 4/4 cells and Tri: 3/3 cells).

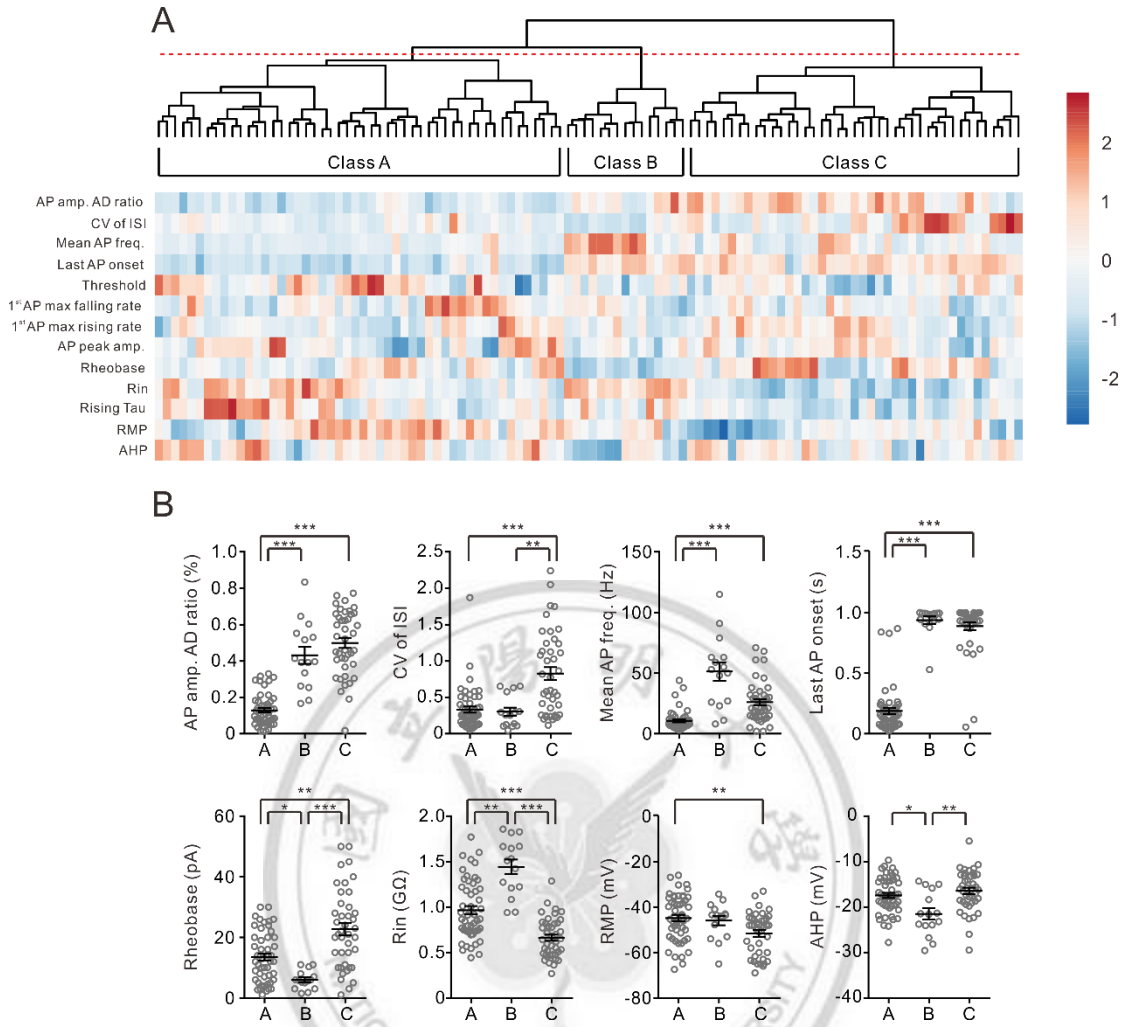

Figure 7. Three electrophysiologically distinct subpopulations of VIP INs

(A) HCA of VIP INs based on active and passive electrophysiological properties. Top, the horizontal-axis of the dendrogram represented the individual cells and the vertical-axis represented the rescaled distance (squared Euclidean, Ward's method) between populations (i.e. A, B, C classes). The dashed line was determined by the result of K-means which was calculated by Silhouette analysis. Bottom, the power of the parameter was shown in the heatmap below the individual cells (see the Materials and Methods in details).

(B) Electrophysiological differences between three neuronal populations (A, 50 cells; B,

15 cells; C, 41 cells). *$p<0.05$; **$p<0.01$; ***$p < 0.001$. Data were expressed as mean ± SEM.

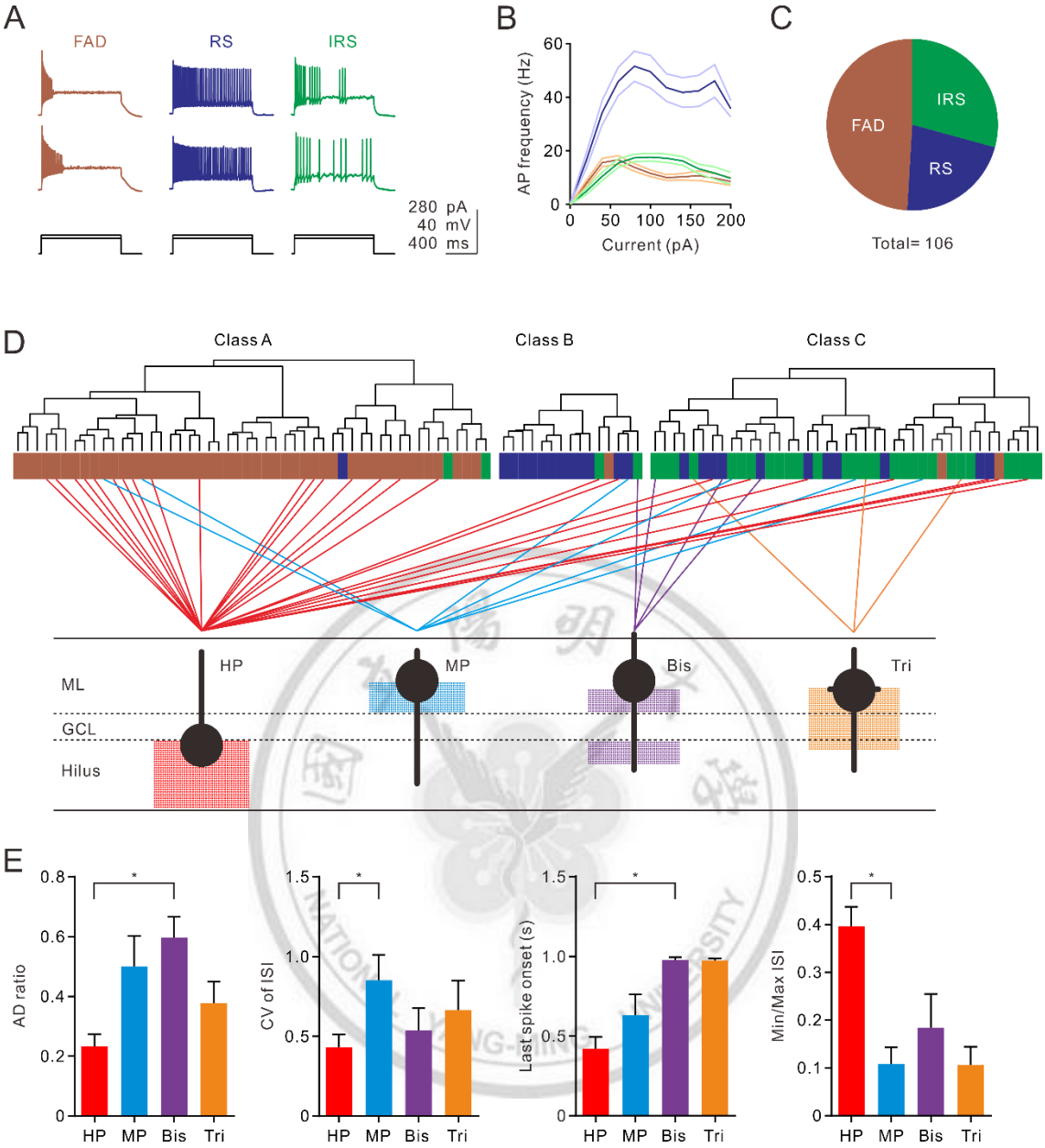

Figure 8. Summary of morpho-electrophysiological classification of VIP INs

(A) Exemplar discharge patterns recorded from fast-adapting (FAD, brown), regular spike (RS, blue) and irregular spike (IRS, green) VIP INs. The FAD, RS and IRS cell types were arbitrarily defined by spike patterns.

(B) The distinct input-output curves of FAD, RS and IRS VIP INs. Current steps were applied in 20 pA increment from 20 to 200 pA.

(C) Summary proportion of FAD, RS and IRS VIP INs.

(D) Relationship between the electrophysiologically determined cell types (A, B, C classes by cluster analysis and FAD, IRS, RS by the arbitrary approach) and morphologically determined cell types (HP, MP, Bis and Tri by the axonal distributions). Color codes below the dendrogram represented FAD (brown), RS (blue) and IRS (green). Lines connected the morphologically distinct cells with electrophysiologically distinct cell types.

(E) Bar graphs summarized active membrane properties in different morphological-defined VIP INs. *$p<0.05$; Data were expressed as mean ± SEM.

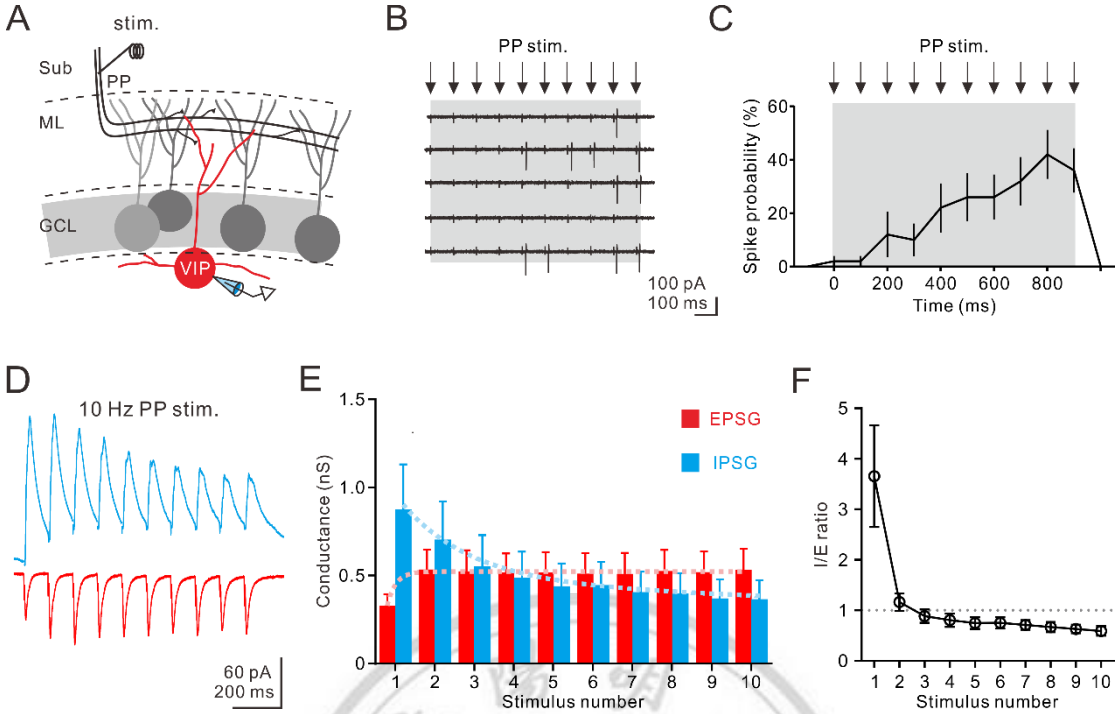

Figure 9. Recruitment of VIP INs by cortical inputs

(A) Schematic diagram showing extracellular stimulation of the perforant path (PP) and recording of VIP INs.

(B) Exemplar cell-attached recording of responses to 10 electrical stimuli. Arrows indicated 10 Hz train stimuli delivered at near-threshold intensities.

(C) Histogram showing spike probability of VIP INs in response to PP stimulation.

(D) EPSCs (red, V_{hold}= -50 mV) and IPSCs (blue, V_{hold}= 0 mV) evoked by 10 Hz electrical stimulation of PP.

(E) Summary of EPSGs and IPSGs during 10 Hz stimulation of PP (n=10). The dash lines were the fits of bi-exponential function.

(F) Summary of the I/E ratio versus the stimulus number during 10 Hz stimulation of PP (n=10). Balanced I/E ratio was indicated by the dashed line.

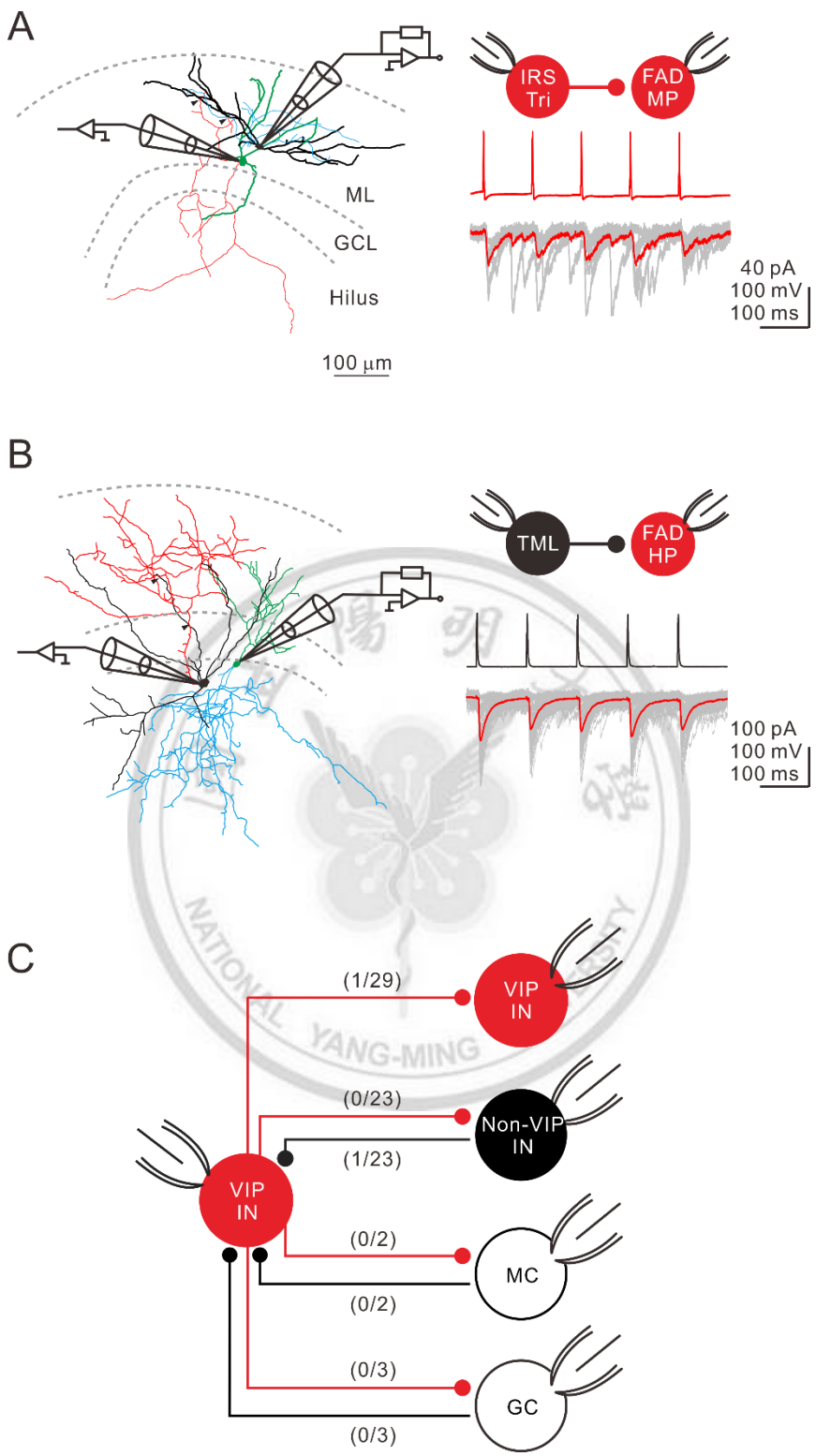
A
ML
GCL
Hilus
100 µm
IRS
Tri
FAD
MP
40 pA
100 mV
100 ms
B
TML
FAD
HP
100 pA
100 mV
100 ms
C
(1/29)
VIP
IN
(0/23)
Non-VIP
IN
(1/23)
VIP
IN
(0/2)
MC
(0/2)
(0/3)
GC
(0/3)

Figure 10. Paired-recording between VIP INs and different types of neurons in the DG

(A and B) Reconstructions of a HP VIP (IRS) IN – MP VIP (FAD) IN pair and a TML-like IN- HP VIP (FAD) IN pair. Soma and dendrites of presynaptic neuron were depicted in black. Axonal arborization of the presynaptic VIP IN was drawn in red. Soma and dendrites of postsynaptic VIP IN were depicted in green. Axonal arborization of the postynaptic VIP IN was drawn in blue. Arrowheads indicated the putative synapses. The presynaptic IN was stimulated by current pulse injection at 10 Hz. Synaptic currents were recorded from INs simultaneously.

(C) Summary of all recorded pairs in the DG.

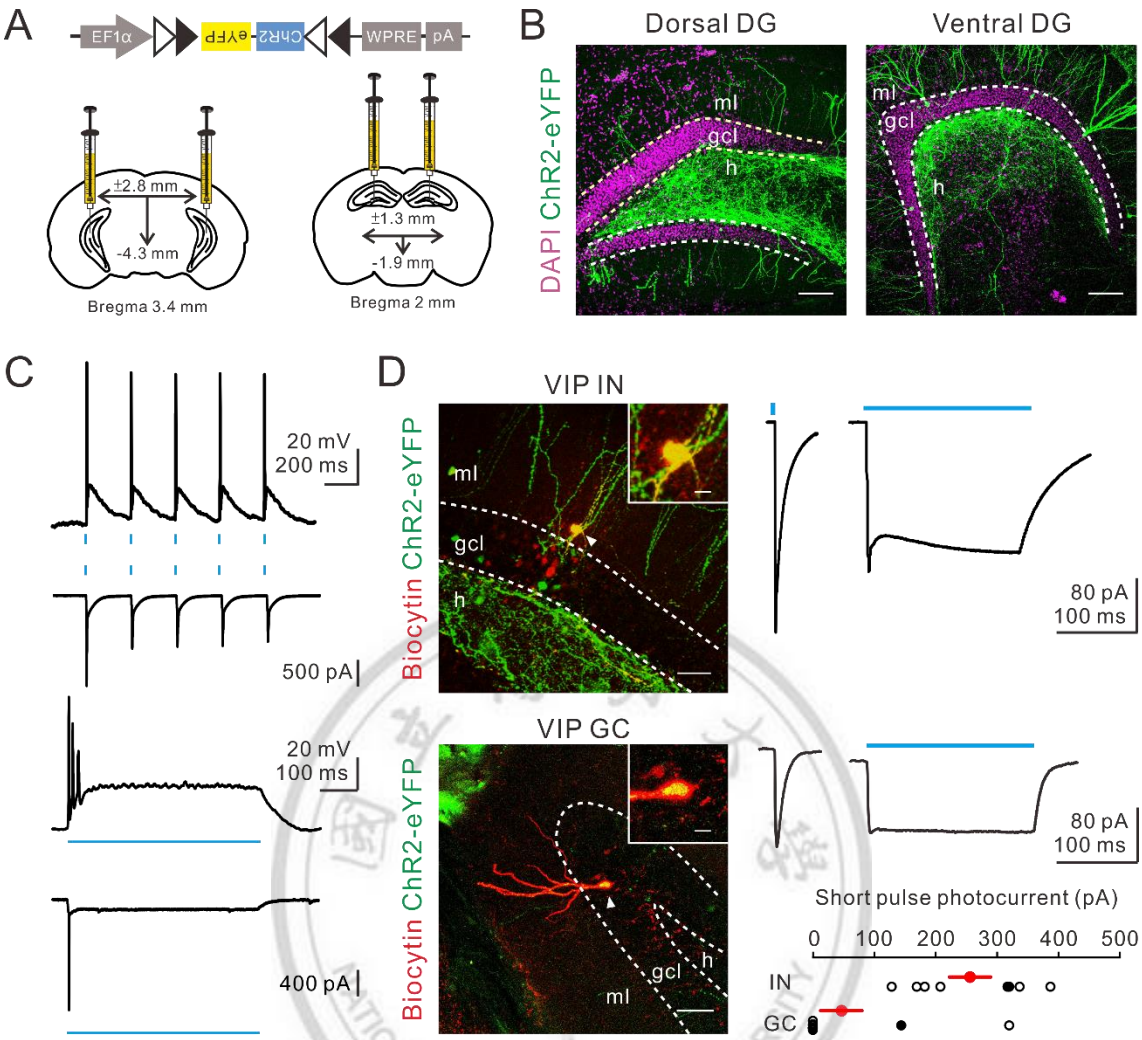

Figure 11. ChR2 expression in the DG VIP neurons

(A) Schematic diagram illustrated the VIP-ires-Cre mouse injected with the viral vector AAV5-EF1α-DIO-ChR2-eYFP into the dorsal or ventral hippocampal DG bilaterally.

(B) ChR2-eYFP and DAPI expression pattern and of the dorsal and ventral DG after 3 weeks of viral delivery. Note dense eYFP signal expressed in the hilus. Scale bar: 100 μm.

(C) Upper, 5-ms light pulses at 5 Hz evoked spikes recorded in an eYFP^{+} IN in current clamp (Ic; holding at -60 mV) and ChR2-mediated photocurrent recorded in voltage clamp (Vc) at -60 mV; Lower, responses of recorded eYFP^{+} INs in both Ic and Vc to 500

ms light stimuli.

(D) Left, the recorded eYFP$^+$ IN (top) and eYFP$^+$ GC (bottom). The arrowheads were shown at a higher magnification in the inset. Scale bar: 50 μm. Scale bar in the inset: 10 μm. Right, the photocurrent evoked by 5- and 200-ms light pulses in the presence of 1 μM TTX. Right, bottom, summary of the peak photocurrent amplitude evoked by 5-ms light pulses. Filled circles represented the photocurrent shown above. Note only 2 out of 8 eYFP$^+$ GCs responded to the photostimulation. Data were expressed as mean ± SEM.

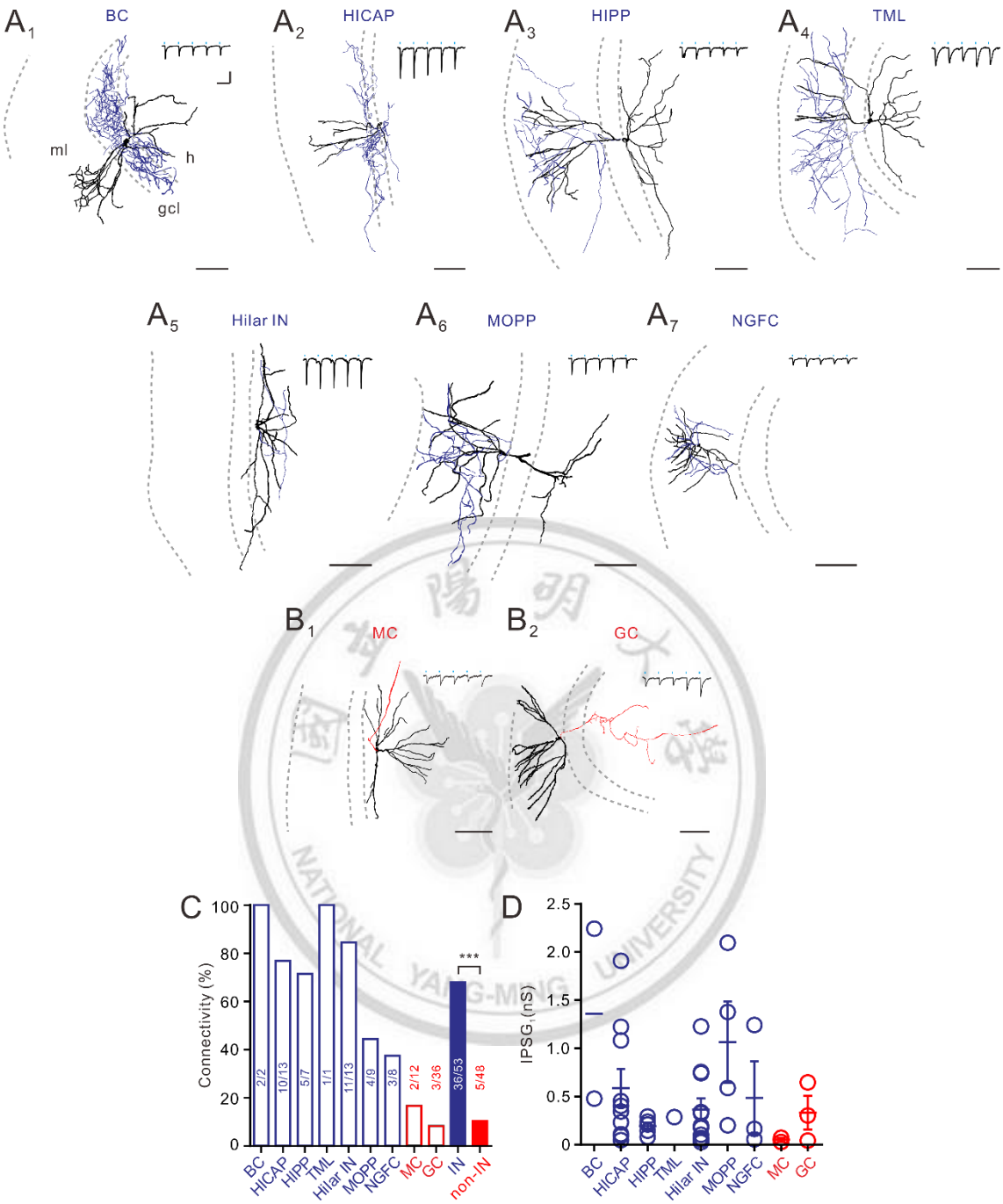

Figure 12. VIP neurons preferentially target INs over excitatory neurons in the DG

(A and B) Exemplar reconstructions and light-evoked IPSCs recorded in different types of neuron in the DG. The dendrites were shown in black. The axons of the inhibitory INs and excitatory neurons were shown in blue and red, respectively. Scale bars: 30 pA, 200 ms, 100 µm.

(C) Connectivity between VIP INs and different types of neurons in the DG (open bars). The overall connectivity between INs and glutamatergic cells were shown in filled bars. Connectivity between VIP to IN and VIP to non-IN was tested by two-tailed Fisher's exact test (IN vs non-IN, ***$p < 0.001$).

(D) Summary of the first IPSG ($IPSG_1$) in different types of light-sensitive postsynaptic neurons. Individual cells were shown in circles. Data were expressed as mean ± SEM.

Table 1. Primary antibodies used in study

Antibody/ Species	Immunogen	Dilution	Source/ Catalog	Reference
VIP (pAb[b]), rabbit	Porcine VIP coupled to bovine thyroglobulin	1:1000	Immunostar, 20077	Prönneke et al., 2015
CR (mAb), mouse	Chick retina, specific for an epitope between amino acids 2-27 at the N-terminus of calretinin	1:300	Santa Cruz, SC-365956	Rizzo et al., 2014
CCK (pAb), rabbit	Synthetic sulfated CCK-8(26-33) amide	1:800	Sigma, C-2581	Tyan et al., 2014
PV (mAb), mouse	Carp-II PV, against PV calcium-bindingprotein of the EF-hand family	1:500	Swant, 10-11 (F)	Donato et al., 2013
SST(mAb), rat	Synthetic 1-14 cyclic somatostatin conjugated to bovine thyroglobulin using carbodiimide.	1:1000	Millipore, MAB354	Marlin et al., 2015

[a] Monoclonal antibody.

[b] Polyclonal antibody.

Table 2. Secondary antibodies used in study

Antibody/Species	Host	Dilution	Source/Catalog#
Alexa Fluor 488 anti-rabbit	Goat	1:500	Invitrogen, A-11008
Alexa Fluor 488 anti-mouse	Goat	1:500	Invitrogen, A-11001
Alexa Fluor 488 anti-rat	Goat	1:500	Invitrogen, A-11006
Alexa Fluor 594 anti-rat	Goat	1:500	Invitrogen, A-11007
Alexa Fluor 633 anti-mouse	Goat	1:500	Invitrogen, A-21052

Table 3. Electrophysiological properties of tdTomato^{+} GCs and INs in the DG

	GCs (16)	INs (106)	p^{a}
AP amp. AD ratio	0.88 ± 0.02	0.32 ± 0.02	<0.001
CV of ISI	0.3 ± 0.03	0.52 ± 0.04	0.32
Mean AP freq. (Hz)	17.3 ± 2	22.4 ± 2.1	0.69
Last AP onset (ms)	956.3 ± 7.4	564.3 ± 39.2	0.003
Threshold (mV)	-34.2 ± 1.7	-36.1 ± 0.6	0.46
1st AP max falling rate (V/s)	89.1 ± 5.5	126.4 ± 4.6	<0.001
Half width (ms)	1	0.79 ± 0.02	<0.001
1st AP max rising rate (V/s)	375.1 ± 31.8	278.6 ± 8.9	0.002
Max AP freq. (Hz)	39.9 ± 3.3	30.6 ± 2.2	0.004
AP peak amplitude (mV)	91 ± 3.3	75.6 ± 1.1	<0.001
Min/Max ISI ratio	0.27 ± 0.04	0.35 ± 0.02	0.45
Rheobase (pA)	34.8 ± 4.5	16 ± 1.1	<0.001
Rin (MΩ)	503.5 ± 53	915.6 ± 37.3	<0.001
Rising Tau (ms)	48.3 ± 4.5	52.9 ± 2.5	0.93
RMP (mV)	-77.1 ± 1.7	-47.6 ± 1	<0.001
AHP (mV)	-13.7 ± 0.6	-17.6 ± 0.4	<0.001

[a] p-value were examined by Mann-Whitney unpaired t-test.

Numbers of cells are given in parentheses. All values are expressed as mean ± SEM

Table 4. Morphological parameters of VIP INs

	HP (27)	MP (6)	Bis (4)	Tri (3)	p^a
Soma					
Perimeter (μm)	36.6 ± 1.2	38.8 ± 3.6	44.2 ± 3.3	37.5 ± 2.4	0.334
Major axis (μm)	12.2 ± 0.3	12.5 ± 0.9	14.9 ± 0.7	12.8 ± 0.2	0.085
Minor axis (μm)	9.1 ± 0.4	9.5 ± 1.2	11.3 ± 1.3	8.7 ± 0.6	0.436
Soma location	0.53 ± 0.02	0.62 ± 0.04	0.77 ± 0.04	0.74 ± 0.08	0.004
Axons					
Total length (mm)	4.3 ± 0.4	3.2 ± 0.2	6 ± 0.3	3.7 ± 1.3	0.19
Total surface (mm^2)	0.28 ± 0.04	0.25 ± 0.04	0.42 ± 0.05	0.24 ± 0.07	0.19
NABP	49.6 ± 5.7	37.7 ± 3.8	81.8 ± 4.4	44.7 ± 13.6	0.07
ASD1[b] (mm)	1 ± 0.2	0.9 ± 0.2	1.7 ± 0.5	1.3 ± 0.4	0.38
ASD2 (mm)	1.9 ± 0.1	1.6 ± 0.2	2.1 ± 0.2	1.3 ± 0.2	0.24
ASD3 (mm)	1.1 ± 0.2	0.7 ± 0.2	1.5 ± 0.2	1 ± 0.5	0.42
ASD4 (mm)	0.43 ± 0.12	0.21 ± 0.08	0.65 ± 0.3	0.23 ± 0.22	0.55
ASD5 (mm)	0.12 ± 0.04	0.09 ± 0.06	0.05 ± 0.05	0	0.76
ASD6 (mm)	0.03 ± 0.02	0.07 ± 0.07	0	0	0.75
ML 100-200 μm (%)	0	3.9 ± 2.8	0	0	0.009
ML 0-100 μm (%)	0.3 ± 0.2	69.2 ± 7.3	15.2 ± 2.8	13 ± 5.2	<0.001
GCL (%)	8.4 ± 2.4	25.6 ± 9.1	38.6 ± 5.9	50.4 ± 8.2	0.01
H 0-100 μm (%)	55.7 ± 3.6	1.3 ± 1.3	44 ± 5.2	34.9 ± 7.9	<0.001
H 100-200 μm (%)	29.6 ± 3.7	0	2.2 ± 1	1.7 ± 1.1	<0.001
H 200-300 μm (%)	5.5 ± 1.3	0	0	0	0.006
H 300-400 μm (%)	0.5 ± 0.3	0	0	0	0.34

Dendrites					
Total length (mm)	2.8 ± 0.2	2.7 ± 0.3	2.9 ± 0.4	3.9 ± 0.2	0.21
Total surface (mm^2)	0.2 ± 0.03	0.19 ± 0.04	0.19 ± 0.03	0.22 ± 0.01	0.54
NDBP	21.4 ± 2.1	20.2 ± 4.6	32.3 ± 4.39	34 ± 4.9	0.06
DSD1[b] (mm)	0.6 ± 0.09	0.6 ± 0.09	0.9 ± 0.2	1.3 ± 0.2	0.06
DSD2 (mm)	0.96 ± 0.1	0.9 ± 0.1	1.3 ± 0.4	1.93 ± 0.26	0.1
DSD3 (mm)	0.7 ± 0.1	0.7 ± 0.1	0.6 ± 0.3	0.5 ± 0.2	0.79
DSD4 (mm)	0.3 ± 0.07	0.3 ± 0.1	0.2 ± 0.1	0.1 ±0.07	0.83
DSD5 (mm)	0.08 ± 0.04	0.1 ± 0.07	0	0	0.35

[a] p-value were examined by Kruskal-Wallis unpaired ANOVA.

[b] ASD, DSD represented the axons or dendrites sholl analysis using Neurolucida Explorer. The numbers indicated every 100 μm as an interval. e.g. DSD1 represented the dendrites length within 0-100 μm far from soma location.

Numbers of cells are given in parentheses. All values are expressed as mean ± SEM

Table 5. Pearson's correlation between the electrophysiological parameters

	Rin	Max. AP freq.	RMP	AHP	Half width	Rheobase	CV of ISI	AP amp. AD ratio	Mean AP freq.	last AP onset	Min/Max ISI	1st AP max rising rate	1st max AP falling rate	Threshold	AP peak	Rising Tau
Rin	1	0.26	0.082	-0.349	0.276	-0.61	-0.33	-0.126	0.223	-0.113	0.294	-0.164	-0.122	-0.033	0.074	0.533
Max. AP freq.	0.26	1	0.039	-0.361	-0.407	-0.341	-0.239	0.251	**0.937**	0.516	0.08	0.392	0.487	-0.227	0.232	-0.121
RMP	0.082	0.039	1	-0.168	-0.226	-0.053	-0.056	-0.234	-0.006	-0.238	0.21	-0.22	0.122	0.098	-0.259	-0.162
AHP	-0.349	-0.361	-0.168	1	0.243	0.174	0.143	-0.103	-0.36	-0.063	-0.192	0.039	-0.349	-0.156	0.023	0.084
Half width	0.276	-0.407	-0.226	0.243	1	-0.045	-0.05	-0.084	-0.37	-0.194	-0.001	-0.471	**-0.79**	-0.028	-0.059	0.473
Rheobase	-0.61	-0.341	-0.053	0.174	-0.045	1	0.224	0.277	-0.244	0.047	-0.145	-0.025	-0.075	0.283	-0.169	-0.416
CV of ISI	-0.33	-0.239	-0.056	0.143	-0.05	0.224	1	0.175	-0.151	0.395	**-0.757**	0.006	0.002	-0.069	0.095	-0.14
AP amp. AD ratio	-0.126	0.251	-0.234	-0.103	-0.084	0.277	0.175	1	0.358	0.67	-0.455	0.31	0.073	-0.001	0.107	-0.145
Mean AP freq.	0.223	**0.937**	-0.006	-0.36	-0.37	-0.244	-0.151	0.358	1	0.657	-0.053	0.357	0.447	-0.225	0.182	-0.151
last AP onset	-0.113	0.516	-0.238	-0.063	-0.194	0.047	0.395	0.67	0.657	1	-0.626	0.318	0.168	-0.184	0.199	-0.168
Min/Max ISI	0.294	0.08	0.21	-0.192	-0.001	-0.145	**-0.757**	-0.455	-0.053	-0.626	1	-0.155	0.048	0.208	-0.241	0.126
1st AP max rising rate	-0.164	0.392	-0.22	0.039	-0.471	-0.025	0.006	0.31	0.357	0.318	-0.155	1	0.609	-0.345	0.596	-0.163
1st max AP falling rate	-0.122	0.487	0.122	-0.349	**-0.79**	-0.075	0.002	0.073	0.447	0.168	0.048	0.609	1	-0.137	0.181	-0.297
Threshold	-0.033	-0.227	0.098	-0.156	-0.028	0.283	-0.069	-0.001	-0.225	-0.184	0.208	-0.345	-0.137	1	-0.536	-0.085
AP peak	0.074	0.232	-0.259	0.023	-0.059	-0.169	0.095	0.107	0.182	0.199	-0.241	0.596	0.181	-0.536	1	0.094
Rising Tau	0.533	-0.121	-0.162	0.084	0.473	-0.416	-0.14	-0.145	-0.151	-0.168	0.126	-0.163	-0.297	-0.085	0.094	1

Table 6. Electrophysiological properties of VIP INs classified by HCA

	A (50)	B (15)	C (41)	*p*-value[a]
AP amp. AD ratio	0.13 ± 0.01	0.43 ± 0.05	0.5 ± 0.03	<0.001
CV of ISI	0.33 ± 0.04	0.3 ± 0.06	0.82 ± 0.09	<0.001
Mean AP freq. (Hz)	10.6 ± 1.2	51.4 ± 7.7	26.1 ± 2.7	<0.001
Last AP onset (ms)	187.6 ± 26.4	937.2 ± 30.8	887.3 ± 32.3	<0.001
Threshold (mV)	-35.6 ± 0.9	-37.1 ± 1	-36.5 ± 0.8	0.69
1st AP max falling rate (V/s)	123.7 ± 7.6	130.9 ± 13.4	127.9 ± 5.7	0.48
Half width (ms)	0.82 ± 0.03	0.76 ± 0.05	0.76 ± 0.02	0.4
1st AP max rising rate (V/s)	57.3 ± 4.2	62.6 ± 6.6	43.9 ± 2.4	0.02
Max AP freq. (Hz)	21.3 ± 1.5	57.7 ± 8.6	32.1 ± 3.3	<0.001
AP peak amplitude (mV)	73.8 ± 1.7	75.3 ± 2.1	78 ± 1.5	0.33
Min/Max ISI ratio	0.49 ± 0.03	0.35 ± 0.06	0.17 ± 0.03	<0.001
Rheobase (pA)	13.5 ± 1.2	6 ± 0.8	22.7 ± 2	<0.001
Rin (GΩ)	964.8 ± 46.5	1442 ± 80.9	663.3 ± 34.3	<0.001
Rising Tau (ms)	57.3 ± 4.2	62.6 ± 6.6	43.9 ± 2.4	0.02
RMP (mV)	-44.9 ± 1.5	-45.9 ± 2.1	-51.6 ± 1.5	0.006
AHP (mV)	-17.4 ± 0.6	-21.5 ± 1.3	-16.5 ± 0.7	0.003

[a] p-value were examined by Kruskal-Wallis unpaired ANOVA.

Numbers of cells are given in parentheses. All values are expressed as mean ± SEM

Table 7. Electrophysiologcial properties of morphological-defined VIP INs

	HP (27)	MP (6)	Bis (4)	Tri (3)	p^a
AP amp. AD ratio	0.23 ± 0.04	0.5 ± 0.1	0.6 ± 0.07	0.38 ± 0.07	0.006
CV of ISI	0.43 ± 0.08	0.85 ± 0.16	0.54 ± 0.14	0.66 ± 0.19	0.01
Mean AP freq. (Hz)	16.2 ± 2.4	10.3 ± 3	25.3 ± 2.5	31 ± 3.6	0.035
Last AP onset (ms)	421.7 ± 72.3	632.6 ± 128.5	979 ± 15.2	974.4 ± 12.2	0.01
Threshold (mV)	-36.2 ± 1	-37.3 ± 1.6	-37.9 ± 2.5	-38.6 ± 3	0.82
1st AP max falling rate (V/s)	119.7 ± 10.3	96.1 ± 11.5	103.3 ± 30.2	113.8 ± 10.2	0.5
Half width (ms)	0.88 ± 0.04	1.04 ± 0.11	0.91 ± 0.11	0.8 ± 0.02	0.35
1st AP max rising rate (V/s)	259.6 ± 16.3	276.5 ± 35.5	303.5 ± 39.8	311.4 ± 25	0.29
Max AP freq. (Hz)	25.2 ± 2.5	12.2 ± 3.2	30.3 ± 4.9	36.3 ± 3.8	0.02
AP peak amplitude (mV)	71.6 ± 2.3	82.9 ± 3.9	75.7 ± 3.2	74.4 ± 3.2	0.23
Min/Max ISI ratio	0.4 ± 0.04	0.11 ± 0.03	0.18 ± 0.07	0.11 ± 0.04	0.002
Rheobase (pA)	15.5 ± 1.9	15.5 ± 5	17.8 ± 5.3	21.7 ± 3.8	0.55
Rin (MΩ)	889.2 ± 73.2	1089 ± 177.6	811.5 ± 154.6	703.4 ± 116	0.56

Rising Tau (ms)	67.5 ±5.9	69.8 ± 14.3	47.8 ± 1.2	57.7 ± 5.1	0.45
RMP (mV)	-47.5 ± 2.2	-49.3 ± 2.7	-60.8 ± 3.8	-53 ± 6.6	0.16
AHP (mV)	-16.4 ± 0.9	-19.4 ± 2.3	-17.2 ± 2	-17.1 ± 0.4	0.56

[a] p-value were examined by Kruskal-Wallis unpaired ANOVA.

Numbers of cells are given in parentheses. All values are expressed as mean ± SEM

Table 8. Properties of light-evoked IPSCs in DG neurons

	Synaptic delay[a] (ms)	20-80% Rise time[b] (ms)	Decay time constant (ms)	$IPSG_1$ (nS)	$IPSG_{1/5}$
BC (2)	6	1.3	37.5	1.4	1.7
HICAP (10)	4.6 ± 0.6	2.2 ± 0.4	21.5 ± 3	0.6 ± 0.2	1.4 ± 0.2
HIPP (5)	3.7 ± 0.8	2.7 ± 0.7	31.6 ± 13.1	0.2	2 ± 0.3
TML (1)	3.2	2.6	35.6	0.3	1.1
Hilar IN (11)	3.9 ± 0.4	2.8 ± 1	26.7 ± 5	0.4 ± 0.1	1.4 ± 0.3
MOPP (3)	6.4 ± 2	2.3 ± 0.4	20.3 ± 3.9	1.4 ± 0.4	3.9 ± 1.2
NGF (3)	5.1 ± 2	2.9 ± 1.7	21.7 ± 5.5	0.5 ± 0.4	1.3 ± 0.2
GC (3)	5.8 ± 0.7	1.4 ± 0.4	21.1 ± 4.4	0.3 ± 0.2	0.6 ± 0.1
MC (2)	2	4.5	21.7	0.05	0.82

[a] Synaptic delay was calculated as the time elapsed from the onset of photo-stimulation to the onset of first monosynaptic EPSC.

[b] 20–80% rise time was measured from the first monosynaptic IPSC

Numbers of cells are given in parentheses. All values are expressed as mean ± SEM

SUPPLEMENTARY FIGURES

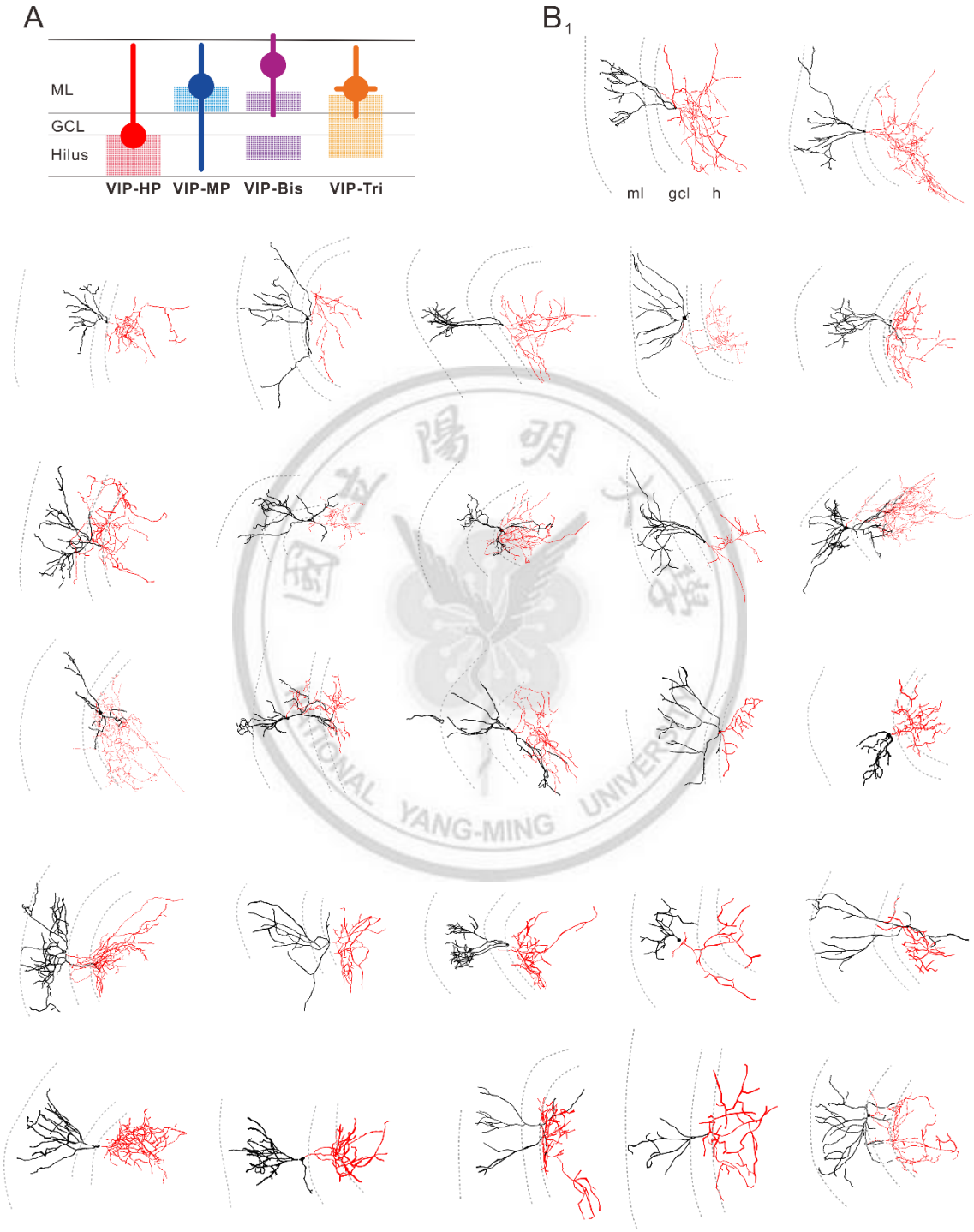

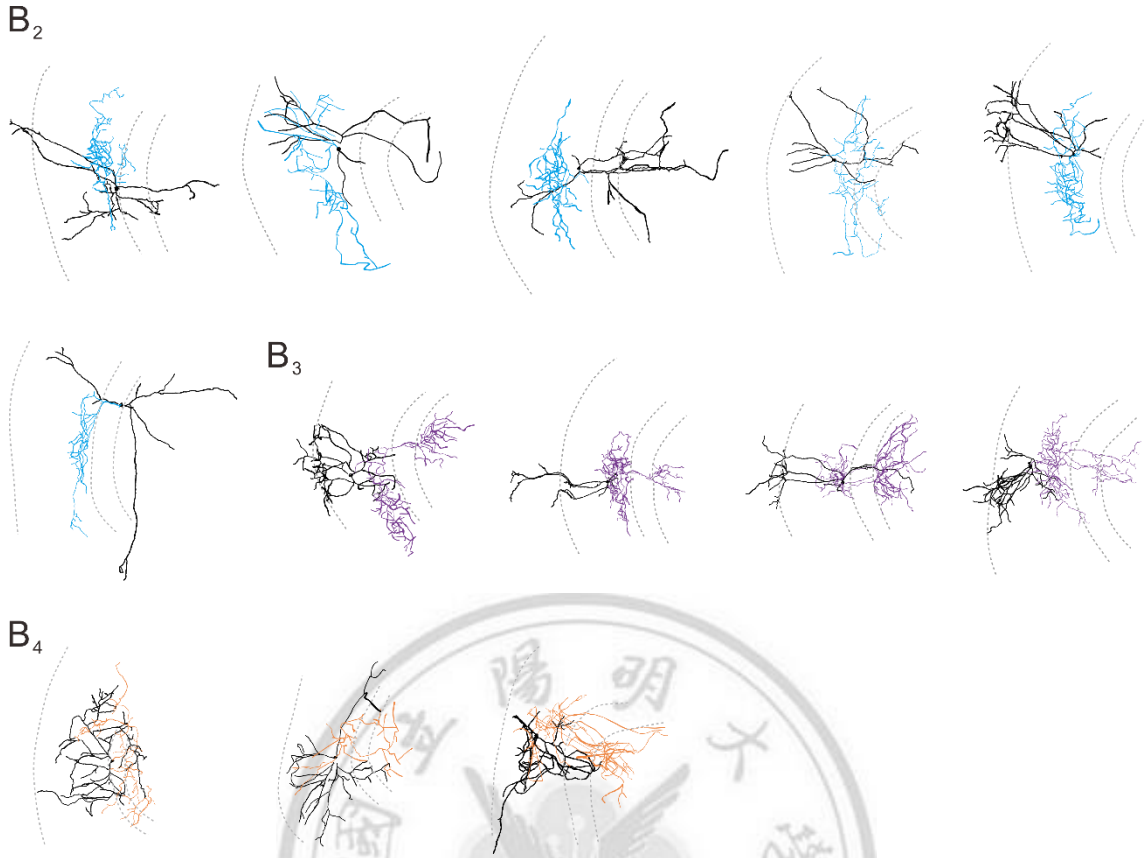

Supplementary Figure 1. Morphological reconstructions of the VIP INs

(A) Scheme of 4 morphologically-defined VIP INs in the DG. Filled circles indicated the soma. The thick rods originated from soma represented the dendrite. The hatched boxes were the domains where the axons arborize. The HP, MP, Bis and Tri VIP INs were depicted in red, blue, purple and yellow, respectively.

(B_1-B_4) All of the 40 reconstructed VIP INs. The dendrites were depicted in black, and the axons were depicted in the same color codes as *(A)*.

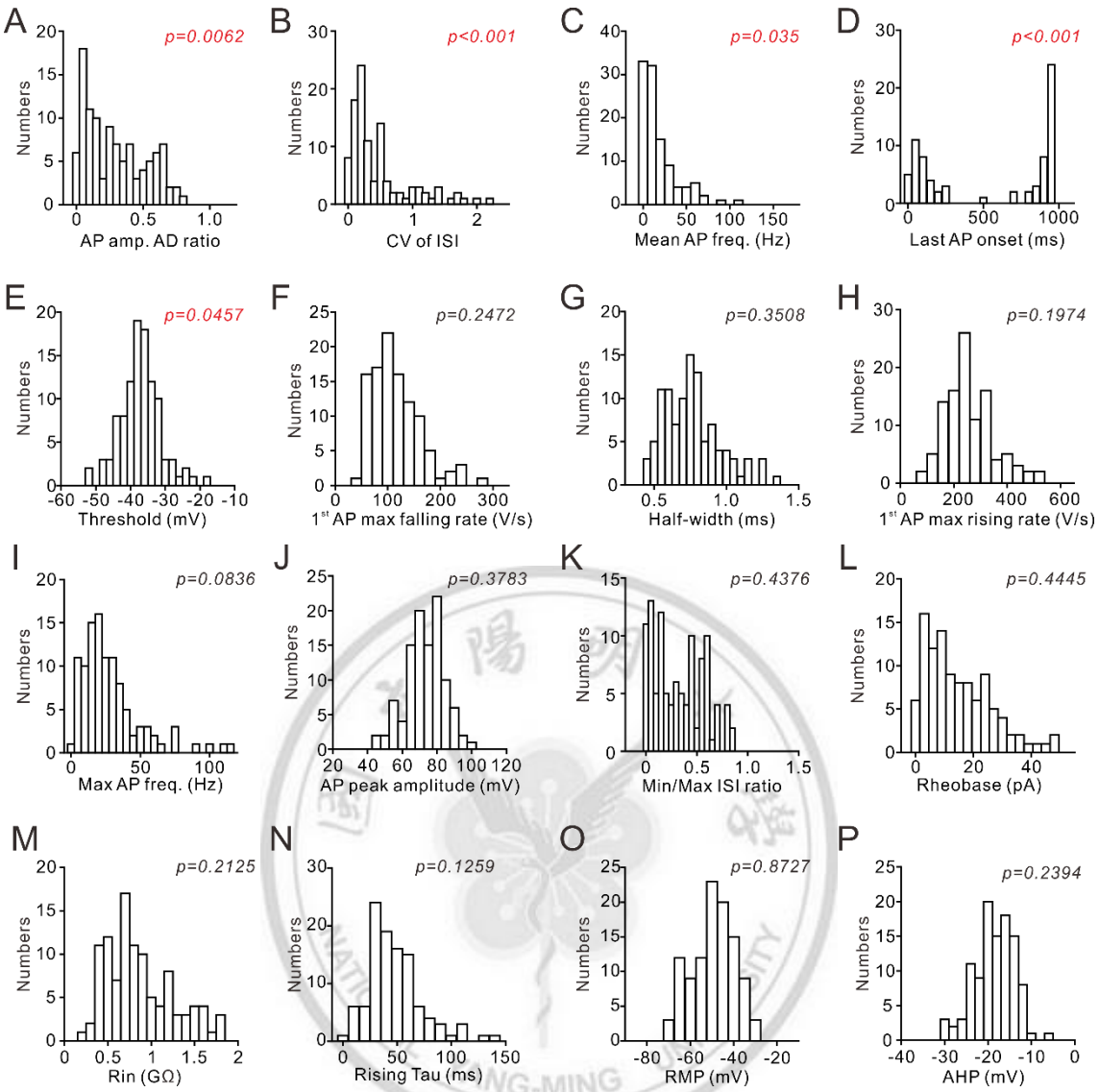

Supplementary Figure 2. Histogram of electrophysiological parameters

(A-P) Histogram of 16 electrophysiologial properties recorded from 106 VIP INs. Note the AD ratio, CV of ISI, mean AP frequency, last AP onset and threshold displayed significantly multimodal distributions. All the variables were binned and tested by D'Agostino Pearson normality test. Red (i.e. $p < 0.05$) indicated non-normal distributions.

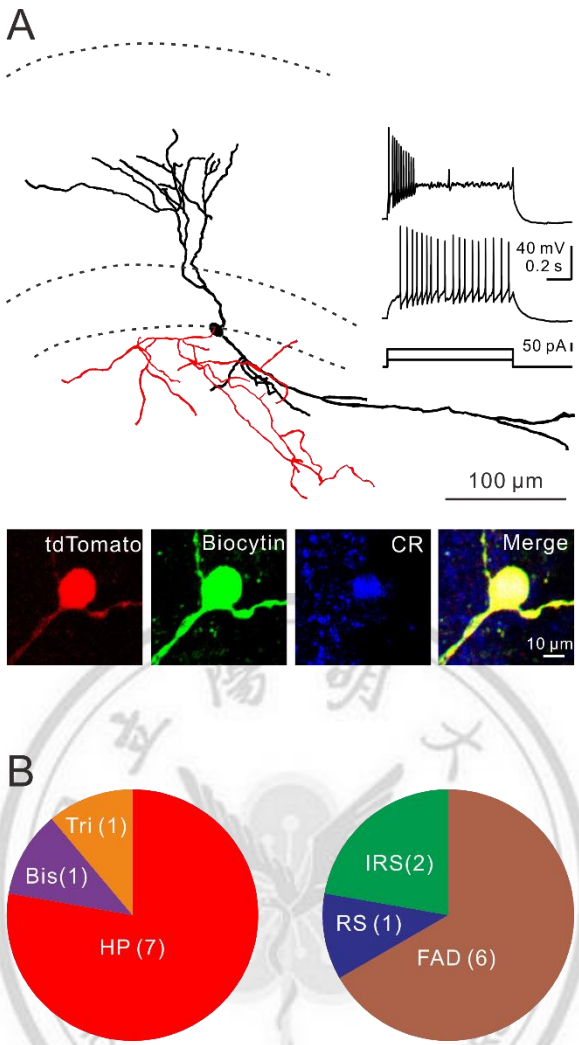

Supplementary Figure 3. Morphological and physiological phenotypes of CR-expressing VIP INs

(*A*) Top, exemplar reconstruction and discharge pattern (+40 and +100 pA depolarizing current injection) of a CR-/VIP-expressing IN. The soma and dendrites were shown in black, the axons were shown in red. Bottom, confocal image stacks showing that a tdTomato^{+} cell (red) with biocytin labeling (green) was immunoreactive for CR (blue).

(*B*) Pie charts illustrating the CR/VIP INs mostly displayed HP morphology (HP, 7/9; Bis, 1/9; Tri, 1/9 cells) and FAD discharge pattern (FAD, 6/9; RS, 1/9; IRS, 2/9 cells).

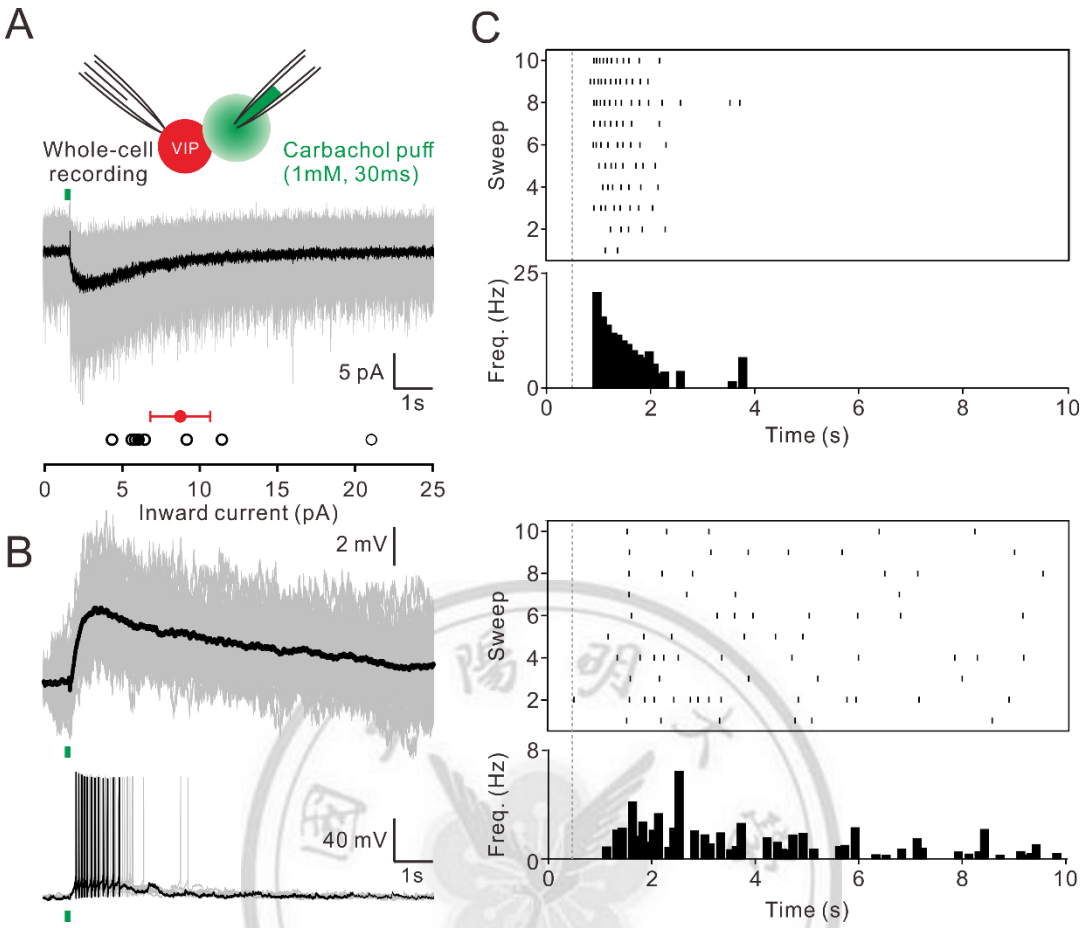

Supplementary Figure 4. Cholinergic activation of VIP INs

(*A*) Top, schematic illustration of carbachol puffing on VIP INs. Bottom, carbachol (1mM) -induced inward currents were recorded in Vc mode (V_{hold} = -60 mV, 8.7 ± 1.9 pA, n = 8). Data were expressed as mean ± SEM.

(*B*) Carbachol application depolarized the membrane potential and evoked bursts of spikes in Ic mode

(*C*) Two exemplar recorded VIP INs in response to carbachol puffs. Top, raster plots indicated the timing of spikes in 10 recording sweeps. Bottom, histograms of firing frequency were plotted in the same time scale as raster plots. Dotted lines represented the onset of puffs

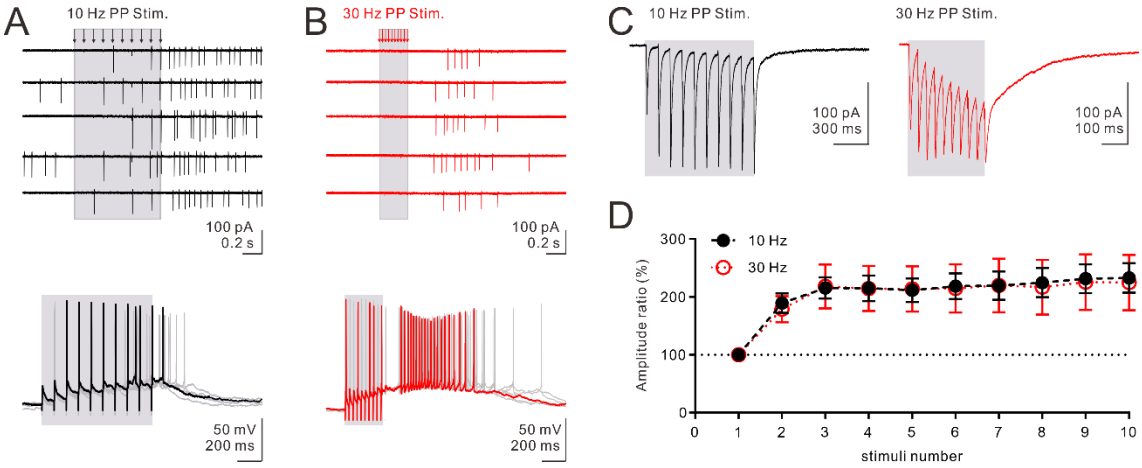

Supplementary Figure 5. Persistent firing of VIP INs after stimulation of PP inputs at theta or gamma frequency

(A and *B)* Top, Exemplar cell-attached recording of responses to 10 Hz (*A*, black) and 30 Hz *(B*, red*)* train stimuli. Arrows indicated 10 stimuli delivered by placing the stimulation electrode in the subiculum. Bottom, spiking probability was detected in Ic mode (V_{hold} around at -75 mV near the Cl^- reversal potential).

(*C*) EPSCs evoked by 10 Hz (black) and 30 Hz (red) PP stimulation (V_{hold}= -75 mV)

(*D*) Summary of normalized EPSCs evoked by during 10 Hz (black) and 30 Hz (red) trains stimuli of PP (n=13). Data were expressed as mean ± SEM.

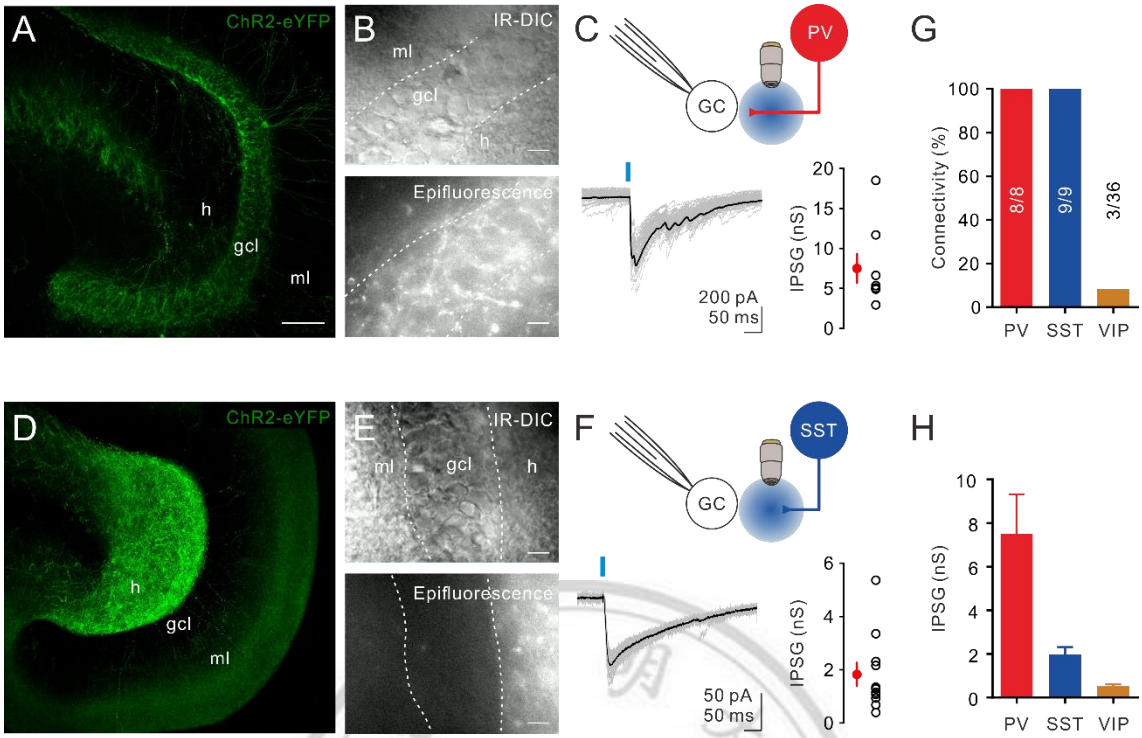

Supplementary Figure 6. Synaptic strength of PV and SST INs in the DG circuitry

(A) ChR2-eYFP expression patterns of the PV-Cre mice. Note the strong expression distributed in perisomatic areas. Scale bar: 100 µm.

(B) Images captured from the IR-DIC and epifluorescence microscope. Note the dense signal was located in the gcl. Scale bar: 10 µm.

(C) Top, schematic illustration of the recording configuration. PV^+ cells were excited by 470 nm light, which was delivered through the objective lens. Bottom, representative IPSCs were recorded from a GC (left), Quantification of IPSG elicited by optogenetic stimulation of PV cells (right). IPSG: 7.5 ± 1.8 nS, n = 8.

(D-F) Same strategies were applied by using SST-Cre mice. IPSG: 1.3 ± 0.2, n = 9. Data were expressed as mean ± SEM.

(*G-H*) Connectivity and IPSG between PV-/SST-/VIP- GC synapses. Data were expressed

as mean ± SEM

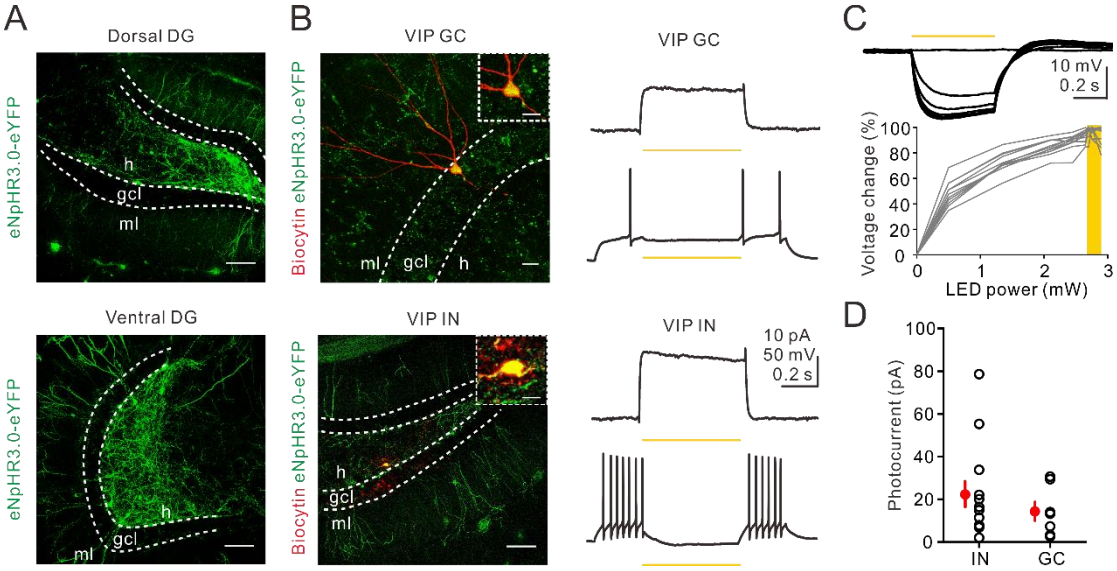

Supplementary Figure 7. Expression and function of eNpHR3.0 in VIP INs and VIP GCs

(A) The expression pattern of an AAV5 carrying EF1α-DIO-eNpHR3.0-eYFP injected into the dorsal (top) and ventral (bottom) DG. Scale bar: 100 µm.

(B) Left, eYFP$^+$ biocytin-filled GCs and INs. Right, the light-evoked photocurrent and optogenetically silencing of VIP-eNpHR$^+$ GC (upper) and IN (lower) in Vc and Ic. Scale bar: 100 µm. Scale bar in boxed area: 10 µm.

(C) Photostimulation of eYFP$^+$ cells with increasing light intensities corresponding to the change of membrane potential (V_{hold} = -60 mV). Representative traces were shown above the input-output curves.

(D) Summary of photocurrent in both eYFP$^+$ IN and eYFP$^+$ GC. Note all of the eYFP$^+$ cells responded to photostimulation. Data were expressed as mean ± SEM.

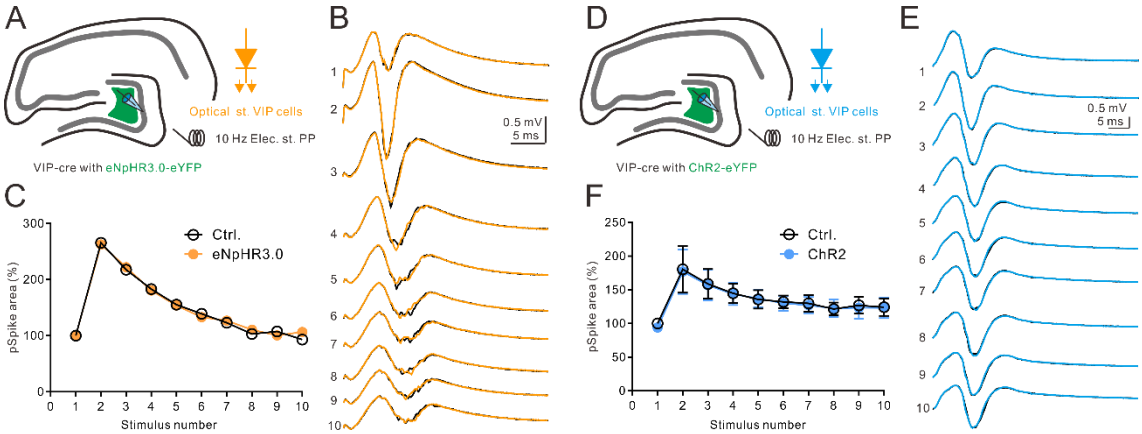

Supplementary Figure 8. Activation or inactivation of VIP INs did not affect the pSpikes of GCs in response to theta PP inputs

(A) Illustration of experimental configuration: A VIP-ires-Cre mouse was injected the AAV5 carrying EF1α-DIO-eNpHR3.0-eYFP (green) into ventral DG. A field recording electrode was placed in the GCL to detect pSpikes. A stimulation electrode was placed in the sub to evoke PP inputs at 10 Hz. pSpikes were monitored under sustained delivery of 590 nm amber light.

(*B*) pSpikes recorded from the GCL under control conditions (black), under light stimulation (amber)

(*C*) Summary of effect of VIP silencing on pSpikes area (the magnitude of pSpike area was normalized to the first pSpike area to PP alone, n = 1). Data were expressed as mean ± SEM.

(*D*) The same strategy was applied in AAV5-EF1α-DIO-ChR2-eYFP injected VIP-ires-Cre mouse. 470 nm, 20 ms blue light was delivered at 10 Hz during the PP stimulation.

(*E*) pSpikes recorded from the GCL under control conditions (black), under light stimulation (blue)

(*F*) Summary of effect of VIP activation on pSpikes area (n = 3). Data were expressed as mean ± SEM.

PROTOCOL OF IMMUNOHITOCHEMISTRY

1. *VIP-ires-Cre::Ai14* mice (age around 1-2 months) are perfused with 4% paraformaldehyde (PFA)/Phosphate buffered saline (PBS), then the brain are permeabilized in the PFA for 2-6 hours at 4℃

2. Replace the PFA with 15% sucrose/PBS for at least 6 hours and then the slices are transferred to 30% sucrose/PBS and stored at 4℃ until sectioning.

3. After sectioning into 60 μm, brain slices are washed using 0.1% Triton X-100 in Tris buffered saline (TBS) for 3 times (10 min each at 4℃)

4. Slices are incubated using 3% H_2O_2/TBS for bleaching (10 min at 4℃)

5. Slices are washed using 0.1% Triton X-100 in Tris buffered saline (TBS) for 3 times (10 min each at 4℃)

6. Slices are incubated in a blocking solution that containing 5% normal goat serum (SP-1000, Vector Labs, Burlingame, CA, USA) or 1-2X animal-free blocker (SP-5030; Vector Labs, Burlingame, CA, USA)/TBS for 2-4 hours at 23-25℃.

7. Slices are incubated with primary antibodies (listed in Table. 1) in the blocking solution for 24-48 hours at 4℃

8. Slices are washed using 0.1% Triton X-100 in TBS for 3 times (10 min each at 4℃), followed by blocking solution with secondary antibodies (listed in Table. 2) incubation for 2-4 hours at 23-25°C

9. Slices are washed six times in TBS for 10 min each, then are mounted in Vectashield with DAPI (H-1500, Vector Labs, Burlingame, CA, USA).